

# Discovery of a topological exciton insulator with tunable momentum order

**Authors:** Md Shafayat Hossain<sup>1\*†</sup>, Tyler A. Cochran<sup>1\*</sup>, Yu-Xiao Jiang<sup>1\*</sup>, Songbo Zhang<sup>2\*</sup>, Huangyu Wu<sup>3, 4\*</sup>, Xiaoxiong Liu<sup>2</sup>, Xiquan Zheng<sup>5</sup>, Byunghoon Kim<sup>1</sup>, Guangming Cheng<sup>6</sup>, Qi Zhang<sup>1</sup>, Maksim Litskevich<sup>1</sup>, Junyi Zhang<sup>7</sup>, Zi-Jia Cheng<sup>1</sup>, Jinjin Liu<sup>3, 4</sup>, Jia-Xin Yin<sup>1</sup>, Xian P. Yang<sup>1</sup>, Jonathan Denlinger<sup>8</sup>, Massimo Tallarida<sup>9</sup>, Ji Dai<sup>9</sup>, Elio Vescovo<sup>10</sup>, Anil Rajapitamahuni<sup>10</sup>, Hu Miao<sup>11</sup>, Nan Yao<sup>6</sup>, Yingying Peng<sup>5</sup>, Yugui Yao<sup>3, 4</sup>, Zhiwei Wang<sup>3, 4†</sup>, Luis Balicas<sup>12</sup>, Titus Neupert<sup>2</sup>, M. Zahid Hasan<sup>1, 6, 13†</sup>

## Affiliations:

<sup>1</sup>Laboratory for Topological Quantum Matter and Advanced Spectroscopy, Department of Physics, Princeton University, Princeton, New Jersey, USA.

<sup>2</sup>Department of Physics, University of Zurich, Winterthurerstrasse, Zurich, Switzerland.

<sup>3</sup>Centre for Quantum Physics, Key Laboratory of Advanced Optoelectronic Quantum Architecture and Measurement (MOE), School of Physics, Beijing Institute of Technology, Beijing 100081, China.

<sup>4</sup>Beijing National Laboratory for Condensed Matter Physics and Institute of Physics, Chinese Academy of Sciences, Beijing 100190, China.

<sup>5</sup>International Center for Quantum Materials, School of Physics, Peking University, Beijing 100871, China.

<sup>6</sup>Princeton Institute for Science and Technology of Materials, Princeton University, Princeton, New Jersey 08544, USA.

<sup>7</sup>Institute for Quantum Matter and Department of Physics and Astronomy, Johns Hopkins University, Baltimore, Maryland 21218, USA.

<sup>8</sup>Advanced Light Source, Lawrence Berkeley National Laboratory.

<sup>9</sup>ALBA Synchrotron Light Source, Cerdanyola del Vallès, 08290 Barcelona, Spain.

<sup>10</sup>National Synchrotron Light Source II, Brookhaven National Laboratory, Upton, New York 11973, USA.

<sup>11</sup>Material Science and Technology Division, Oak Ridge National Laboratory, Oak Ridge, Tennessee 37830, USA.

<sup>12</sup>National High Magnetic Field Laboratory, Tallahassee, Florida 32310, USA.

<sup>13</sup>Lawrence Berkeley National Laboratory, Berkeley, California 94720, USA.

†Corresponding authors, E-mail: mdsh@princeton.edu; zhiweiwang@bit.edu.cn; mzh Hasan@princeton.edu.

\*These authors contributed equally to this work.

## Abstract

**Topology and correlations are fundamental concepts in modern physics, but their simultaneous occurrence within a single quantum phase is exceptionally rare. In this study, we present the discovery of such a phase of matter in  $Ta_2Pd_3Te_5$ , a semimetal where the Coulomb interaction between electrons and holes leads to the spontaneous formation of excitonic bound states below  $T \simeq 100$  K. Our spectroscopy unveils the development of an insulating gap stemming from the condensation of these excitons, thus giving rise to a highly sought-after correlated quantum phase known as the excitonic insulator. Remarkably, our scanning tunneling microscopy measurements reveal the presence of gapless boundary modes in the excitonic insulator state. Their magnetic field response and our theoretical calculations suggest a topological origin of these**

**modes, rendering  $\text{Ta}_2\text{Pd}_3\text{Te}_5$  as the first experimentally identified topological excitonic insulator in a three-dimensional material not masked by any structural phase transition. Furthermore, our study uncovers a secondary excitonic instability below  $T \simeq 5$  K, which differs from the primary one in having finite momentum. We observe unprecedented tunability of its wavevector by an external magnetic field. These findings unlock a frontier in the study of novel correlated topological phases of matter and their tunability.**

## **Main text**

In the pursuit of new collective phases of matter that exhibit intriguing quantum properties, one long-standing goal has been the realization of the excitonic insulator. The excitonic insulator, initially proposed in theoretical studies dating back to 1965, is an exotic state where excitons spontaneously form and undergo Bose-Einstein condensation in thermodynamic equilibrium<sup>1-4</sup>. This elusive phenomenon has attracted significant attention due to its possible unique characteristics, such as dissipationless energy transport akin to a superfluid<sup>5</sup>, electronic ferroelectricity<sup>6</sup>, and superradiant emission<sup>7</sup>. Formally, the excitonic insulator shares similarities with superconductors, as both involve many-body effects beyond noninteracting electron theory and the spontaneous emergence of a condensate of paired fermions. In the case of the excitonic insulator, the condensate is formed by excitons, which are bound electron-hole pairs<sup>8,9</sup>. While the excitonic insulator is primarily driven by electronic interactions, it is often accompanied by a structural phase transition<sup>3,10</sup>, leaving many experimental signatures ambiguous. Among the three-dimensional materials considered as potential excitonic insulators<sup>11-16</sup>, the most promising candidate so far,  $\text{Ta}_2\text{NiSe}_5$ , experiences such a structural transition<sup>10,17-19</sup>. Consequently, whether  $\text{Ta}_2\text{NiSe}_5$  truly hosts an excitonic insulator state remains a subject of debate<sup>10</sup>. On the other hand, two-dimensional systems, such as bilayer heterostructures under high magnetic fields<sup>20-25</sup> and materials like  $\text{WTe}_2$ <sup>26,27</sup>, have shown indications of exciton condensation. In the case of  $\text{WTe}_2$ , exciton condensation is observed exclusively in the monolayer form<sup>26,27</sup>, while the three-dimensional  $\text{WTe}_2$  becomes a metal without an energy gap<sup>28,29</sup>. Here, we report the discovery of an excitonic insulator phase in a three-dimensional material  $\text{Ta}_2\text{Pd}_3\text{Te}_5$ , which is free from any structural phase transition. In this material, our data indicates that excitons spontaneously form, leading to the development of a bulk-gapped excitonic insulator state. Remarkably, our study unveils that this correlated insulating state features a boundary mode (edge state) consistent with the topological bulk-boundary correspondence, rendering  $\text{Ta}_2\text{Pd}_3\text{Te}_5$  as the first experimentally identified topological excitonic insulator in a three-dimensional material. Furthermore, our spectroscopic investigation reveals that this highly exotic state is susceptible to a secondary excitonic instability, whose wavevector can be tuned by external magnetic field.

Our investigation begins by characterizing the atomic structure of  $\text{Ta}_2\text{Pd}_3\text{Te}_5$ , which adopts an orthorhombic phase with the space group  $\text{Pnma}$  (No. 62)<sup>30</sup>. The atomic arrangement and Brillouin zone of  $\text{Ta}_2\text{Pd}_3\text{Te}_5$  are schematically illustrated in Figs. 1a and 1b, respectively. The unit cell comprises two  $\text{Ta}_2\text{Pd}_3\text{Te}_5$  monolayers that are stacked along the  $a$ -axis through weak van der Waals interactions. Each monolayer encompasses a Ta-Pd mixed layer sandwiched between two Te layers. To confirm the pristine atomic structure of our  $\text{Ta}_2\text{Pd}_3\text{Te}_5$  sample, we conducted detailed atomic imaging on the (010) and (001) surfaces using scanning transmission electron microscopy (Extended Fig. 1). The obtained results confirm the expected lattice parameters of  $\text{Ta}_2\text{Pd}_3\text{Te}_5$ , with values of  $a = 14.08$  Å,  $b = 3.72$  Å, and  $c = 18.66$  Å, which are consistent with previous investigations<sup>30</sup>. Elemental mapping using an energy-dispersive X-ray detector (Extended Fig. 2) demonstrates unperturbed atomic layers, affirming the structural integrity and composition of  $\text{Ta}_2\text{Pd}_3\text{Te}_5$ . Furthermore, selected area electron diffraction patterns acquired at temperatures of 290 K (top) and 90 K (bottom) (Extended Fig. 1) exhibit identical crystal symmetries, underscoring the absence of a structural phase transition in  $\text{Ta}_2\text{Pd}_3\text{Te}_5$  within this temperature range (also see Extended Fig. 3 for X-ray diffraction results elaborated on below). Figure 1c presents an atomically resolved scanning tunneling

microscopy topographic image of a freshly cleaved Ta<sub>2</sub>Pd<sub>3</sub>Te<sub>5</sub> (100) surface, revealing a quasi-one-dimensional chain of Te atoms extending along the  $b$ -axis. A magnified topographic image with atomic resolution is presented in the bottom inset of Fig. 1c, corroborating the structural model of Ta<sub>2</sub>Pd<sub>3</sub>Te<sub>5</sub> presented in Fig. 1a. The Fourier-transformed image in the top inset of Fig. 1c displays well-defined Bragg peaks that correspond to lattice constants of approximately 3.7 Å and 18.6 Å, in agreement with the lattice constants along the  $b$ - and  $c$ -axes, respectively.

Having identified a pristine surface, we conducted spectroscopic measurements. The spatially-averaged differential conductance ( $dI/dV$ ) spectra acquired at different temperatures are presented in Fig. 1d. At higher temperatures ( $T \gtrsim 100$  K), the system exhibits a gapless, semimetallic state, as evident from the nearly-V-shaped  $dI/dV$  spectrum with low but non-zero local density of states at the Fermi energy. However, an insulating gap emerges at  $T \lesssim 100$  K (Extended Fig. 4) and gradually increases in magnitude as the sample is cooled (Fig. 1e). We also measured the development of this insulating energy gap with angle-resolved photoemission spectroscopy, by exploiting matrix-element selection effects (Extended Fig. 5) and temperature control. A photoemission spectrum acquired at  $T = 160$  K reveals a semimetallic nature (Fig. 1f, left panel), as evidenced by the presence of spectral intensity all the way up to the Fermi level at the  $\bar{\Gamma}_2$  point (Fig. 1f, left panel). Whereas at  $T = 15$  K, the spectrum reveals a clear energy gap at the Fermi energy (Fig. 1f, right panel). Moreover, we find that the spectral weight at the valence band edge increases dramatically at low temperatures, as exemplified by the development of a sharp coherence peak at the gap edge (Fig. 1g). (Note that the position of the photoemission coherence peak relative to the Fermi energy is approximately -50 meV, which notably aligns with the tunneling spectroscopy-derived location of the valence band edge close to -50 meV.) The appearance of such a spectral feature upon gap development is reminiscent of superconductivity and points to the existence of a correlated phase.

To understand the insulating transition at 100 K and the development of a coherence peak at the gap edge, we conducted polarization-dependent angle-resolved photoemission spectroscopy measurements. This approach leverages linearly polarized X-rays to provide an orbital fingerprint of the electronic states<sup>31-33</sup>. Particularly, band hybridization between bands of distinct orbital character is detectable as a change in the photoemission intensity for certain light polarizations. We orient the sample, such that the  $\bar{\Gamma} - \bar{Z}$  path lies within the scattering plane, ensuring that photoelectrons at the  $\bar{\Gamma}_2$  point are not affected by any experimental asymmetry. We measured energy/momentum slices of the Brillouin zone along the  $\bar{\Gamma}_2 - \bar{Y}_2$  path with s- and p-polarized light at 160 K and 15 K (Fig. 2a-d). Here, s and p designate light with an electric field perpendicular and parallel to the plane of incidence, respectively. s-polarization yields a strongly suppressed spectral weight at the  $\bar{\Gamma}_2$  point, consistent with a plane-wave final state<sup>32</sup>; no spectral weight at the Fermi level is discernable in our s-polarized measurements at 160 K (Fig. 2a). This spectrum is also insensitive to lowering the temperature to 15 K (Fig. 2c). However, considering the p-polarized spectrum, we observe a notable spectral weight at the  $\bar{\Gamma}_2$  point at 160 K (Fig. 2b). Remarkably, the 15 K p-polarized spectrum shows a substantial increase in spectral weight near the Fermi level, consistent with the results in Fig. 1f and indicating significant temperature-dependent coupling to another degree of freedom in the system (Fig. 2d). To explain this strong coherence feature, we turn to *ab initio* band structure calculations for the orbital composition of the bare bands. Because our angle-resolved photoemission spectroscopy measurements at the  $\bar{\Gamma}_2$  point have a finite out-of-plane momentum resolution and the Brillouin zone dimensions are small in the  $k_a$  direction ( $0.45 \text{ \AA}^{-1}$ ), we consider all states along the  $\Gamma - X$  line (Fig. 2e). Near the Fermi level, there are four bands. The orbital local xyz coordinate system is defined as follows: the x-direction along the in-plane  $b$ -axis, the y-direction along the in-plane  $c$ -axis, and the z-direction along the surface-normal  $a$ -axis. With this convention, the lower two “valence” bands, primarily possess  $d_{x^2-y^2}$ ,  $d_{yz}$ , and  $d_{z^2}$  character, while the upper two “conduction”

bands stem mostly from  $d_{xy}$ ,  $d_{xz}$ , and  $p_x$  orbitals. All four bands carry negligible  $p_y$ ,  $p_z$ , and  $s$  weight. Returning to our photoemission results, the polarization-dependent spectra can be explained by the interaction between electrons and holes. Such coupling hybridizes the conduction and valence bands, which, in turn, can generate a coherence feature. While any  $d_{xy}$  contribution to the spectral intensity of the valence band is unlikely due to orbital symmetry, the significant  $d_{xz}$  and  $p_x$  weight of the conduction band is allowed considerable spectral intensity because the  $\bar{\Gamma}_2$  point is away from normal emission in the scattering plane<sup>32</sup>. Within this framework, the hybridization between the conduction and valence bands (stemming from electron-hole interaction) would lead to an enhanced signal in photoemission spectra, as the valence band acquires more  $d_{xz}$ , and  $p_x$  character.

It is crucial to emphasize that the emergence of the insulating gap *is not* a result of a structural phase transition. As previously discussed, our electron diffraction results indicate no structural phase change occurring near  $T \simeq 100$  K when the insulating gap appears. Moreover, we conducted X-ray diffraction measurements at various temperatures, ranging from  $T = 300$  K to 20 K, as shown in Extended Fig. 3. These measurements unequivocally reveal the absence of any structural phase transition, even down to 20 K. Furthermore, we do not observe any symmetry breaking when the gap opens. Specifically, there is no superlattice modulation or translation symmetry breaking present near  $T = 100$  K and even at  $T = 5$  K (see Fig. 1c; also Fig. 4a,b as discussed later). An alternative scenario for gap formation is a Mott insulating state. However,  $\text{Ta}_2\text{Pd}_3\text{Te}_5$  is a semimetal at temperatures above 100 K which is distinct from a typical Mott picture where, prior to Mott transition, the system is metallic with commensurate filling. Therefore, most likely, based on the discussion above, the coherence feature in Fig. 1g is due to conduction band-valence band hybridization stemming from electron-hole interaction, in other words, from the formation of an exciton condensate with zero momentum that preserves the space group symmetries. This condensate lowers the energy of the system by opening a gap seen in both tunneling and photoemission measurements (Fig. 2f).

These observations in  $\text{Ta}_2\text{Pd}_3\text{Te}_5$  contrast with the scenario for  $\text{Ta}_2\text{NiSe}_5$ , where a structural phase transition coincides with the exciton formation. This concurrence raises questions about the origin of the insulating gap in  $\text{Ta}_2\text{NiSe}_5$ : is it driven by electronic interactions or the structural transition<sup>10, 17-19</sup>? Recent studies have concluded that the insulating gap in  $\text{Ta}_2\text{NiSe}_5$  is primarily structural in nature and not the result of exciton condensation<sup>10</sup>. In contrast,  $\text{Ta}_2\text{Pd}_3\text{Te}_5$  does not exhibit such complexities, as it lacks a structural phase transition and translation symmetry breaking (discussed in detail in Fig. 4), and the insulating gap is most likely a consequence of exciton condensation.

Having discussed the spontaneous formation and condensation of excitons into a correlated insulating state, our attention turns to investigating the topological properties of this correlated state. A hallmark of topology is the presence of gapless boundary states protected by time-reversal symmetry within the insulating bulk energy gap. To explore these boundary states, we conducted real-space investigations using scanning tunneling microscopy, which allows for direct, atomic-scale visualization with high spatial and energy resolution<sup>34</sup>. This powerful technique has proven effective in identifying topological boundary states in various quantum materials<sup>34-46</sup>. Upon scanning a freshly cleaved  $\text{Ta}_2\text{Pd}_3\text{Te}_5$  crystal, we observe a well-defined monolayer atomic step edge along the  $b$ -axis, as identified by the topographic image and corresponding height profile in Fig. 3a. Remarkably, our spatially resolved spectroscopic imaging at  $T = 5$  K reveals a pronounced edge state within the correlated insulating gap, as depicted by the differential conductance ( $dI/dV$ ) maps at  $V = 0$  mV and 30 mV in Fig. 3a (see Extended Fig. 6 for additional results). To characterize the spatial profile of the edge state, we extract a line profile from the  $dI/dV$  map, as illustrated in Fig. 3b. The line profile demonstrates an exponential decay of the edge state along the crystal side, with a characteristic decay length of  $r_0 \simeq 1.6$  nm, indicating an exponential localization of the edge state. The edge

state exhibits a steeper decay on the vacuum side. Furthermore, energy-resolved spectroscopic measurements conducted on the step edge (Fig. 3c) reveal a substantial  $dI/dV$  signal (represented by orange curves) around the Fermi energy, while the  $dI/dV$  spectrum away from the step edge (violet curves) exhibits an insulating gap.

To test the topological nature of the observed boundary state, we investigate its response to an external magnetic field. The magnetic field breaks the time-reversal symmetry that protects the gapless topological edge states. When a magnetic field perpendicular to the  $bc$  plane is applied, we observe a significant suppression of the  $dI/dV$  measured at the step edge. The field-dependent tunneling spectra, shown for  $B = 2$  T, 3 T, and 6 T in Fig. 3c, demonstrate a gradual formation of an insulating gap at the edge state. (The field-induced suppression of the edge state is also visualized in the  $dI/dV$  map under  $B = 6$  T, depicted in Fig. 3d.) The emergence of this gap at the step edge bears resemblance to a Zeeman gap, which typically stems from the field-induced coupling of helical edge states in a time-reversal symmetric material<sup>47-49</sup>. Notably, a clear and reasonably linear increase of the energy gap in both the terrace (bulk) and the step edge is observed when plotting the energy gap magnitude derived from the field-dependent tunneling spectra as a function of the magnetic field (Fig. 3e), thus corroborating the anticipated behavior of the Zeeman effect. Attributing the gap only to the Zeeman effect provides an estimate for the  $g$ -factors of bulk and edge, which are 9 and 70, respectively. It is worth noting that these  $g$ -factor estimates also include the effect of orbital magnetization. Furthermore, since the bulk energy gap is due to interactions, its magnitude may be affected by the magnetic field, leading to a nonlinear dependence of the gap on  $B$  that cannot be characterized by an effective  $g$ -factor alone. Overall, the observed edge state, initially gapless and located within the bulk insulating energy gap, undergoes a transition to a gapped state when subjected to a time-reversal-symmetry-breaking perturbation, providing compelling evidence for its protection by the time-reversal symmetry, a characteristic hallmark of topological boundary states<sup>50, 51</sup>.

Additionally, we conducted temperature-dependent tunneling measurements to examine the behavior of the edge state as the bulk insulating gap closes above the exciton insulator transition temperature. The results of these experiments, depicted in Fig. 3f, demonstrate that the insulating bulk gap and the prominent edge state observed at  $T = 5$  K disappears at  $T = 120$  K. At  $T = 120$  K, the bulk reverts to a gapless, semimetallic state, while the edge state becomes suppressed in  $dI/dV$  magnitude compared to the bulk. This temperature-dependent transition of the quantum state of the bulk and edge is also evident in the spatially resolved spectroscopic maps shown in Fig. 3g. At  $T = 5$  K, the  $dI/dV$  maps taken at the Fermi energy display a pronounced state at the edge, and no discernible state at the bulk, whereas at  $T = 120$  K, the bulk states become more prominent than the edge. We refer the reader to Extended Fig. 6 for additional results on the observation of the time-reversal-symmetry-protected edge state in  $\text{Ta}_2\text{Pd}_3\text{Te}_5$ .

The presence of a topological boundary mode within the correlated exciton insulator energy gap indicates that the ground state of the material is likely a topological exciton insulator, representing the first observation of this elusive quantum phase in a three-dimensional material. Next, we cool the sample further to examine the excitonic state at lower temperatures. Figure 4a displays a large-area topographic image and corresponding  $dI/dV$  maps of the occupied (-200 mV) and unoccupied (100 mV) sides of the insulating gap obtained at  $T = 5$  K. As alluded to in earlier discussions, in this zero momentum exciton condensate, no superlattice modulations in the charge distribution are observed, and only the Bragg peaks are visible in the respective Fourier transform images (Fig. 4a,b). Strikingly, however, at an even lower temperature of  $T = 4.2$  K, a secondary spontaneous electronic transition that *does* break translation symmetry with incommensurate wavevector is observed, clearly visualized through the topographic image in Fig. 4c, with the corresponding Fourier transform image displaying distinct peaks

denoted as  $Q_{\text{exc}}$ . By spatially mapping the  $dI/dV$  on both the occupied (-200 mV) and unoccupied (100 mV) sides of the energy gap, we spectroscopically visualize the resulting superlattice modulations, demonstrating spectroscopic contrast stemming from the superlattice modulation (Fig. 4c). Interestingly, the local density of states maxima (minima) at -200 mV correspond to local density of states minima (maxima) at 100 mV, indicating a reversal of the spectroscopic contrast, consistent with a translation symmetry breaking order. Moreover, peaks at wavevectors  $Q_{\text{exc}}$  obtained from the Fourier transform of the  $dI/dV$  maps coincide with those from the Fourier transform of the topography (Fig. 4c). Additionally, we investigated the energy dependence of the wavevectors  $Q_{\text{exc}}$ , and found that they appear to be energy-independent, as the  $Q_{\text{exc}}$  peak locations remain non-dispersive outside of the insulating gap (Fig. 4d). (Note that within the insulating gap, by definition, no discernible spectroscopic signal is present.)

To understand the nature of the translation breaking order formed within the primary exciton insulator state, we have performed magnetic field dependence studies (Fig. 4e,f and Extended Fig. 7). In Extended Fig. 7, a series of topographic images acquired at various magnetic fields (0 T, 2 T, 4 T, and 6 T) at  $T = 4.2$  K clearly reveal the presence of translation symmetry breaking at all fields. Interestingly, the corresponding wavevectors ( $Q_{\text{exc}}$ ) continuously change with increasing magnetic field, as visualized by the Fourier transform of the topography. This field-induced evolution of  $Q_{\text{exc}}$  is further evidenced by the spectroscopic imaging presented in Fig. 4e, revealing spectroscopic contrast in real space on both the occupied and unoccupied sides of the energy gap, with a contrast reversal between the two sides, akin to the zero-field data in Fig. 4c. Importantly, the  $Q_{\text{exc}}$  peaks obtained from the Fourier transforms of the  $dI/dV$  maps align with those obtained from the Fourier transform of the topography (Fig. 4e), both revealing markedly different  $Q_{\text{exc}}$  peak positions compared to the zero-field data. The field-induced evolution of  $Q_{\text{exc}}$ , as summarized in Fig. 4f (also refer to Extended Fig. 7f), provides crucial insights into the nature of the ordering. At high temperatures (above  $T \approx 100$  K),  $\text{Ta}_2\text{Pd}_3\text{Te}_5$  is a semimetal with an indirect band crossing where particle- and hole-band extrema are separated by a finite, non-zero wavevector in the Brillouin zone. The primary exciton condensate is expected to inherit this characteristic wavevector in its effective (mean-field) band structure. The secondary order should then be interpreted as another exciton condensate with this nonzero wavevector, which manifests as the periodicity of the excitonic superlattice modulation in real space. As the magnetic field induces a continuous shift in the particle- and hole-bands due to the Zeeman effect, the wavevector of the secondary excitonic order should also change continuously with increasing magnetic field, which is precisely what we observe in our experiments, strongly supporting the excitonic character of the secondary order<sup>52</sup>.

Furthermore, we have substantiated the bulk nature of the excitonic order using systematic transport experiments. Our transport experiments (Extended Fig. 8) support the overall scanning tunneling microscopy observations as well as the related conclusions. We observe clear electric threshold fields  $E_{\text{th}}$  for non-linear carrier conduction, due to the sliding or phason mode of the translation symmetry breaking excitonic order<sup>53</sup>, only below  $T \cong 5$  K. Satellite peaks, associated with the finite momentum exciton condensate, become observable in the Fourier transform of the scanning tunneling microscopy images precisely in this range of temperatures. The absence of both, translation symmetry breaking in scanning tunneling microscopy images, and non-linear electrical conduction, confirms the absence of a translation symmetry breaking order and the zero momentum nature of the electron-hole condensate observed above  $T \cong 5$  K. Furthermore,  $E_{\text{th}}$  continuously changes with the magnetic field, aligning with our scanning tunneling microscopy results (see Methods section XIII for details).

To better understand the two exciton condensation orders that we discovered in  $\text{Ta}_2\text{Pd}_3\text{Te}_5$ , we formulated a two-band minimum model on a square lattice (see Methods). With an appropriate choice of parameters, the model can

mimic the low-energy band structure of monolayer  $\text{Ta}_2\text{Pd}_3\text{Te}_5$  obtained in first-principles calculations (Extended Fig. 9). In its high-temperature phase, the system has no (indirect) global gap, with the conduction band minimum situated around the  $M$  point ( $\mathbf{k} = (0, \pi)$ ) and slightly below (by approximately 7 meV) the valence band maxima located along the  $k_y = 0$  line (Fig. 5a,b). The model has an inverted band structure consistent with density functional theory calculations and angle resolved photoemission spectroscopy measurements. Due to a direct gap at all momenta, it can be characterized by a topological invariant which is nontrivial. Consequently, under open boundary conditions, the system exhibits edge states which, however, are buried by the bulk continuum (Fig. 5c). To account for the two excitonic instabilities, we incorporate long-range Coulomb interaction and apply Hartree-Fock mean-field approximation to the model. We initially identify that the primary excitonic order, which involves the pairing of electrons and holes with identical momentum, emerges at low temperatures ( $T \leq 100$  K) via a second order phase transition as the temperature decreases. This leads to a substantial global bulk energy gap (Fig. 5d, e, f), which grows monotonically as the temperature is lowered (Fig. 5g). As the excitonic order strengthens, the direct gap between the conduction and valence bands is maintained (Fig. 5h). Consequently, the topological properties of the model are not changed by the primary excitonic order, evident in the persistence of gapless edge states across the bulk insulating gap under open boundary conditions (Fig. 5f), consistent with experimental findings. Under the excitonic instability, the conduction band minimum and the valence band maxima remain well separated in momentum space. This separation is what triggers the formation of a secondary excitonic order, where the ordering wave vector  $Q$  is equal to the momentum separation of the conduction band minimum and valence band maxima. We theoretically model this secondary transition by using the mean-field band structure resulting from the primary zero momentum excitonic order. Next, we self-consistently solve for the secondary excitonic order with finite momentum (marked in Fig. 5f). While breaking translation symmetry, this order does not change the system's topology (which is protected by time-reversal symmetry alone) and only minimally increases the bulk gap (Fig. 5i, j, k, l), aligning with experimental observations. Note that the secondary exciton order corresponds to a large momentum transfer in the Coulomb interaction and happens on top of a sizable insulating gap. This makes the secondary excitonic order weaker than the primary one, resulting in a lower critical temperature. We further accounted for Zeeman coupling that may arise due to externally applied magnetic fields in our calculations. We find that this Zeeman term can smoothly change the momentum separation between the conduction band minimum and valence band maxima (Fig. 5m), which is consistent with the change of the ordering wave vector under the application of magnetic fields.

The discovery of a topological excitonic insulator, which combines topological edge states with spontaneous exciton condensation, represents a breakthrough in the study of correlated topological phases of matter. Finding two such consecutive transitions in the same material (Fig. 5n), one with zero and one with finite momentum (that is tunable via an external magnetic field) is unprecedented and invites new studies to make innovative optoelectronic/optical devices using these excitons. Furthermore, unraveling this material platform opens the door to investigating the intriguing interplay between non-trivial band topology and quantum many-body effects. Additionally, the parallels between excitonic insulators and superconductors prompt the anticipation of exciting developments, potentially emulating the physics of topological superconductors, which is another highly sought-after phase, within our newly discovered topological excitonic insulator state.

## References

1. Keldysh, L. & Kopayev, Y. Possible instability of semimetallic state toward Coulomb interaction. *Sov. Phys. Sol. State* **6**, 2219–2224 (1964).

2. Cloizeaux, J. D. Exciton instability and crystallographic anomalies in semiconductors. *J. Phys. Chem. Solids* **26**, 259–266 (1965).
3. Jerome, D., Rice, T. M. & Kohn, W. Excitonic insulator. *Phys. Rev.* **158**, 462–475 (1967).
4. Halperin, B. I. & Rice, T. M. Possible anomalies at a semimetal–semiconductor transition. *Rev. Mod. Phys.* **40**, 755–766 (1968).
5. Snoke, D. Spontaneous Bose coherence of excitons and polaritons. *Science* **298**, 1368–1372 (2002).
6. Batista, C. D., Gubernatis, J. E., Bonča, J. & Lin, H. Q. Intermediate coupling theory of electronic ferroelectricity. *Phys. Rev. Lett.* **92**, 187601 (2004).
7. Mazza, G. & Georges, A. Superradiant quantum materials. *Phys. Rev. Lett.* **122**, 017401 (2019).
8. Safaei, S. & Mazziotti, D. A. Quantum signature of exciton condensation. *Phys. Rev. B* **98**, 045122 (2018).
9. Schouten, A. O., Sager-Smith, L. M. & Mazziotti, D. A. Large cumulant eigenvalue as a signature of exciton condensation. *Phys. Rev. B* **105**, 245151 (2022).
10. Baldini, E. et al. The spontaneous symmetry breaking in Ta<sub>2</sub>NiSe<sub>5</sub> is structural in nature. *Proc. Natl Acad. Sci., USA* **120**, e2221688120 (2023).
11. Rohwer, T. et al. Collapse of long-range charge order tracked by time-resolved photoemission at high momenta. *Nature* **471**, 490–493 (2011).
12. Kogar, A. et al. Signatures of exciton condensation in a transition metal dichalcogenide. *Science* **358**, 1314–1317 (2017).
13. Lu, Y. F. et al. Zero-gap semiconductor to excitonic insulator transition in Ta<sub>2</sub>NiSe<sub>5</sub>. *Nat. Commun.* **8**, 14408 (2017).
14. Werdehausen, D. et al. Coherent order parameter oscillations in the ground state of the excitonic insulator Ta<sub>2</sub>NiSe<sub>5</sub>. *Sci. Adv.* **4**, eaap8652 (2018).
15. Varsano, D. et al. Carbon nanotubes as excitonic insulators. *Nat. Commun.* **8**, 1461 (2017).
16. Ataei, S. S., Varsano, D., Molinari, E. & Rontani, M. Evidence of ideal excitonic insulator in bulk MoS<sub>2</sub> under pressure. *Proc. Natl Acad. Sci.* **118**, e2010110118 (2021).
17. Mazza, G. et al. Nature of symmetry breaking at the excitonic insulator transition: Ta<sub>2</sub>NiSe<sub>5</sub>. *Phys. Rev. Lett.* **124**, 197601 (2020).
18. Subedi, A. et al. Orthorhombic-to-monoclinic transition in Ta<sub>2</sub>NiSe<sub>5</sub> due to a zone-center optical phonon instability. *Phys. Rev. Mater.* **4**, 083601 (2020).
19. Watson, M. D. et al. Band hybridization at the semimetal–semiconductor transition of Ta<sub>2</sub>NiSe<sub>5</sub> enabled by mirror-symmetry breaking. *Phys. Rev. Res.* **2**, 013236 (2020).
20. Eisenstein, J. P. & MacDonald, A. H. Bose–Einstein condensation of excitons in bilayer electron systems. *Nature* **432**, 691–694 (2004).
21. Nandi, D., Finck, A. D. K., Eisenstein, J. P., Pfeiffer, L. N. & West, K. W. Exciton condensation and perfect Coulomb drag. *Nature* **488**, 481–484 (2012).
22. Li, J. I. A., Taniguchi, T., Watanabe, K., Hone, J. & Dean, C. R. Excitonic superfluid phase in double bilayer graphene. *Nat. Phys.* **13**, 751–755 (2017).
23. Liu, X., Watanabe, K., Taniguchi, T., Halperin, B. I. & Kim, P. Quantum Hall drag of exciton condensate in graphene. *Nat. Phys.* **13**, 746–750 (2017).
24. Du, L. et al. Evidence for a topological excitonic insulator in InAs/GaSb bilayers. *Nat Commun* **8**, 1971 (2017).
25. Wang, R. et al. Excitonic topological order in imbalanced electron–hole bilayers. *Nature* **619**, 57–62 (2023).
26. Jia, Y. et al. Evidence for a monolayer excitonic insulator. *Nat. Phys.* **18**, 87–93 (2022).



27. Sun, B. *et al.* Evidence for equilibrium exciton condensation in monolayer WTe<sub>2</sub>. *Nat. Phys.* **18**, 94–99 (2022).
28. Ali, M. *et al.* Large, non-saturating magnetoresistance in WTe<sub>2</sub>. *Nature* **514**, 205–208 (2014).
29. Soluyanov, A. *et al.* Type-II Weyl semimetals. *Nature* **527**, 495–498 (2015).
30. Wang, X. *et al.* Observation of topological edge states in the quantum spin Hall insulator Ta<sub>2</sub>Pd<sub>3</sub>Te<sub>5</sub>. *Phys. Rev. B* **104**, L241408 (2021).
31. Damascelli, A., Hussain, Z. & Shen, Z.-X. Angle-resolved photoemission studies of the cuprate superconductors. *Rev. Mod. Phys.* **75**, 473 (2003).
32. Moser, S. An experimentalist's guide to the matrix element in angle resolved photoemission, *Journal of Electron Spectroscopy and Related Phenomena.* **214**, 29-52 (2017).
33. Matt, C.E., Sutter, D., Cook, A.M. *et al.* Direct observation of orbital hybridisation in a cuprate superconductor. *Nat Commun* **9**, 972 (2018).
34. Yin, J. -X., Pan, S. H. & Hasan, M. Z. Probing topological quantum matter with scanning tunnelling microscopy. *Nat. Rev. Phys.* **3**, 249 (2021).
35. Yang, F. *et al.* Spatial and energy distribution of topological edge states in single Bi(111) bilayer. *Phys. Rev. Lett.* **109**, 016801 (2012).
36. Drozdov, I. K. *et al.* One-dimensional topological edge states of bismuth bilayers. *Nat. Phys.* **10**, 664–669 (2014).
37. Pauly, C. *et al.* Subnanometre-wide electron channels protected by topology. *Nat. Phys.* **11**, 338–343 (2015).
38. Wu, R. *et al.* Evidence for topological edge states in a large energy gap near the step edges on the surface of ZrTe<sub>5</sub>. *Phys. Rev. X* **6**, 021017 (2016).
39. Li, X.-B. *et al.* Experimental observation of topological edge states at the surface step edge of the topological insulator ZrTe<sub>5</sub>. *Phys. Rev. Lett.* **116**, 176803 (2016).
40. Wang, Z. *et al.* Topological edge states in a high-temperature superconductor FeSe/SrTiO<sub>3</sub>(001) film. *Nat. Mater.* **15**, 968–973 (2016).
41. Sessi, P. *et al.* Robust spin-polarized midgap states at step edges of topological crystalline insulators. *Science* **354**, 1269–1273 (2016).
42. Peng, L. *et al.* Observation of topological states residing at step edges of WTe<sub>2</sub>. *Nat. Commun.* **8**, 659 (2017).
43. Liu, S. *et al.* Experimental observation of conductive edge states in weak topological insulator candidate HfTe<sub>5</sub>. *APL Mater.* **6**, 121111 (2018).
44. Ugeda, M. M. *et al.* Observation of topologically protected states at crystalline phase boundaries in single-layer WSe<sub>2</sub>. *Nat. Commun.* **9**, 3401 (2018).
45. Liu, R. Z. *et al.* Experimental observations indicating the topological nature of the edge states on HfTe<sub>5</sub>. *Chin. Phys. Lett.* **36**, 117301 (2019).
46. Shumiya, N. *et al.* Evidence of a room-temperature quantum spin Hall edge state in a higher-order topological insulator. *Nat. Mater.* **21**, 1111–1115 (2022).
47. Shi, Y., *et al.* Imaging quantum spin Hall edges in monolayer WTe<sub>2</sub>. *Sci. Adv.* **5**, eaat8799 (2019).
48. Dominguez, F., *et al.* Testing topological protection of edge states in hexagonal quantum spin Hall candidate materials. *Phys. Rev. B* **98**, 161407(R) (2018).
49. Fu, Y. S. *et al.* Observation of Zeeman effect in topological surface state with distinct material dependence. *Nat Commun* **7**, 10829 (2016).
50. Qi, X.-L. & Zhang, S.-C. Topological insulators and superconductors. *Rev. Mod. Phys.* **83**, 1057 (2011).

51. Bernevig, B. A. & Hughes, T. L. Topological Insulators and Topological Superconductors (Princeton University Press, 2013).
52. Chen, C., Singh, B., Lin, H. & Pereira, V. M. Reproduction of the Charge Density Wave Phase Diagram in 1T-TiSe<sub>2</sub> Exposes its Excitonic Character. *Phys. Rev. Lett.* **121**, 226602 (2018).
53. Grüner, G. The dynamics of charge-density waves. *Rev. Mod. Phys.* **60**, 1129–1181 (1988).

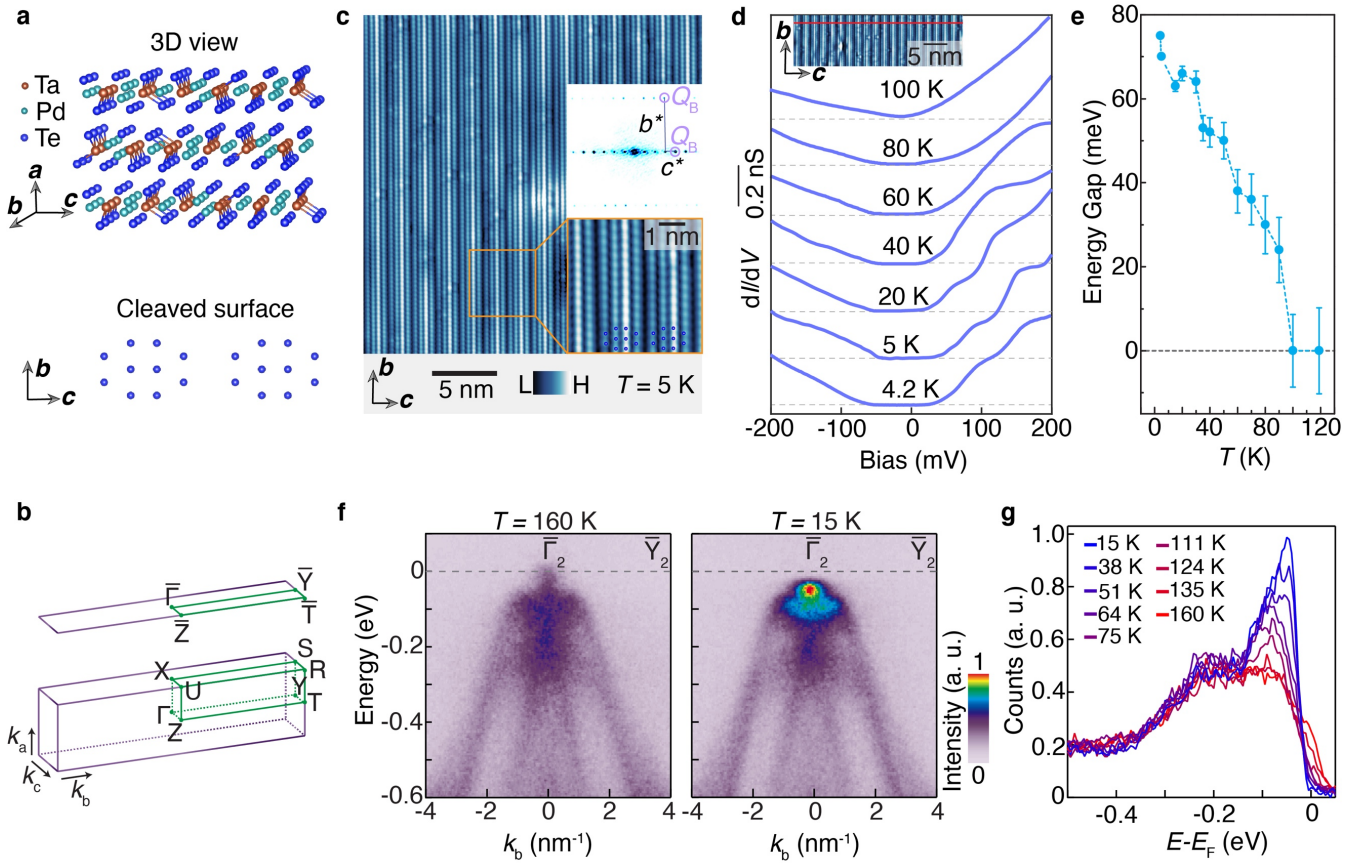


**Fig. 1: Real and reciprocal space characterization of Ta<sub>2</sub>Pd<sub>3</sub>Te<sub>5</sub> showing the development of an insulating bulk gap around  $T = 100$  K.** **a**, Crystal structure (top panel) and the cleaved (100) surface (bottom panel). **b**, Brillouin zone for Ta<sub>2</sub>Pd<sub>3</sub>Te<sub>5</sub> with  $k_c < k_a < k_b$  (bottom panel) and the surface Brillouin zone with surface normal perpendicular to the cleave plane (top panel). High symmetry points and lines are marked in green. **c**, Atomically resolved scanning tunneling microscopy topographic image of the (100) plane ( $V_{\text{set}} = 300$  mV,  $I_{\text{set}} = 0.5$  nA). **d**, Spatially averaged energy-resolved tunneling spectra obtained at various temperatures. Spectra are averaged along the red line marked in the topographic image (inset). Spectra for different temperatures are vertically offset for clarity. No gap is observed in the  $dI/dV$  spectrum at  $T = 100$  K, while at  $T = 4.2$  K, a sizeable insulating gap of approximately 75 meV emerges. **e**, Temperature dependence of the insulating gap. The gap appears around 100 K and enlarges with decreasing temperature. Vertical bars indicate the thermal broadening energy for each data point. **f**, Photoemission energy vs momentum spectra along the  $\bar{\Gamma}_2 - \bar{Y}_2$  path at  $T = 162$  K (left) and 14 K (right), acquired using 50 eV, p-polarized incident light. At  $T = 162$  K, the spectral weight extends above the Fermi level,

marked by the dotted black line. However, at  $T = 14$  K, an energy gap appears at the Fermi energy. Notably, the spectral weight at the valence band edge dramatically increases. **g**, Photoemission energy-distribution curves taken at the  $\bar{\Gamma}_2$  point, collected using 50 eV, p-polarized incident X-rays. High-temperature traces (red) have a value above the background while crossing the Fermi energy. As temperature decreases, a gap appears at the Fermi level, and a coherence feature develops at low temperatures (blue).

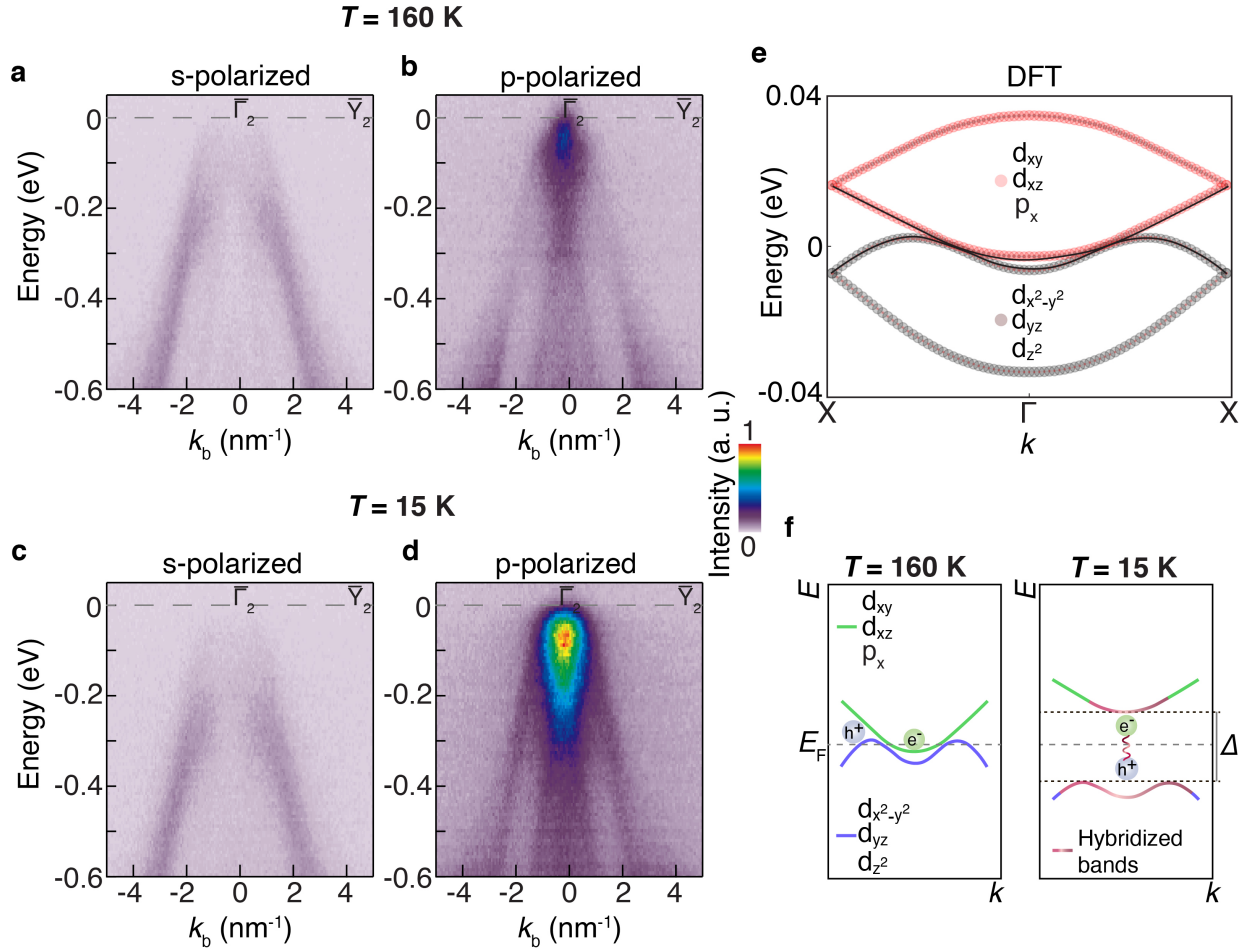


**Fig. 2: Revealing spontaneously formed excitons at low temperatures through the orbital character of hybridized bands.** **a-d**, Angle-resolved photoemission spectra measured along the  $\bar{\Gamma}_2 - \bar{\Gamma}_2$  direction at  $T = 160$  K (panels **a**, **b**) and at  $T = 15$  K (panels **c**, **d**). s-polarized incident light was used for panels **a** and **c**, while p-polarized light was used for panels **b** and **d**. **e**, *Ab initio* calculation of the band structure along the  $\Gamma - X$  line. Black translucent circles correspond to the cumulative  $d_{x^2-y^2}$ ,  $d_{yz}$ , and  $d_{z^2}$  orbital contributions. Red translucent circles represent the cumulative  $d_{xy}$ ,  $d_{xz}$ , and  $p_x$  orbital contributions.  $p_y$ ,  $p_y$ , and  $s$  orbitals carry negligible weight. **f**, Schematic band structures illustrating the mechanism behind the formation of an exciton insulator, where hybridization between holes in the conduction band and electrons in the valence band gives rise to an exciton insulator state.

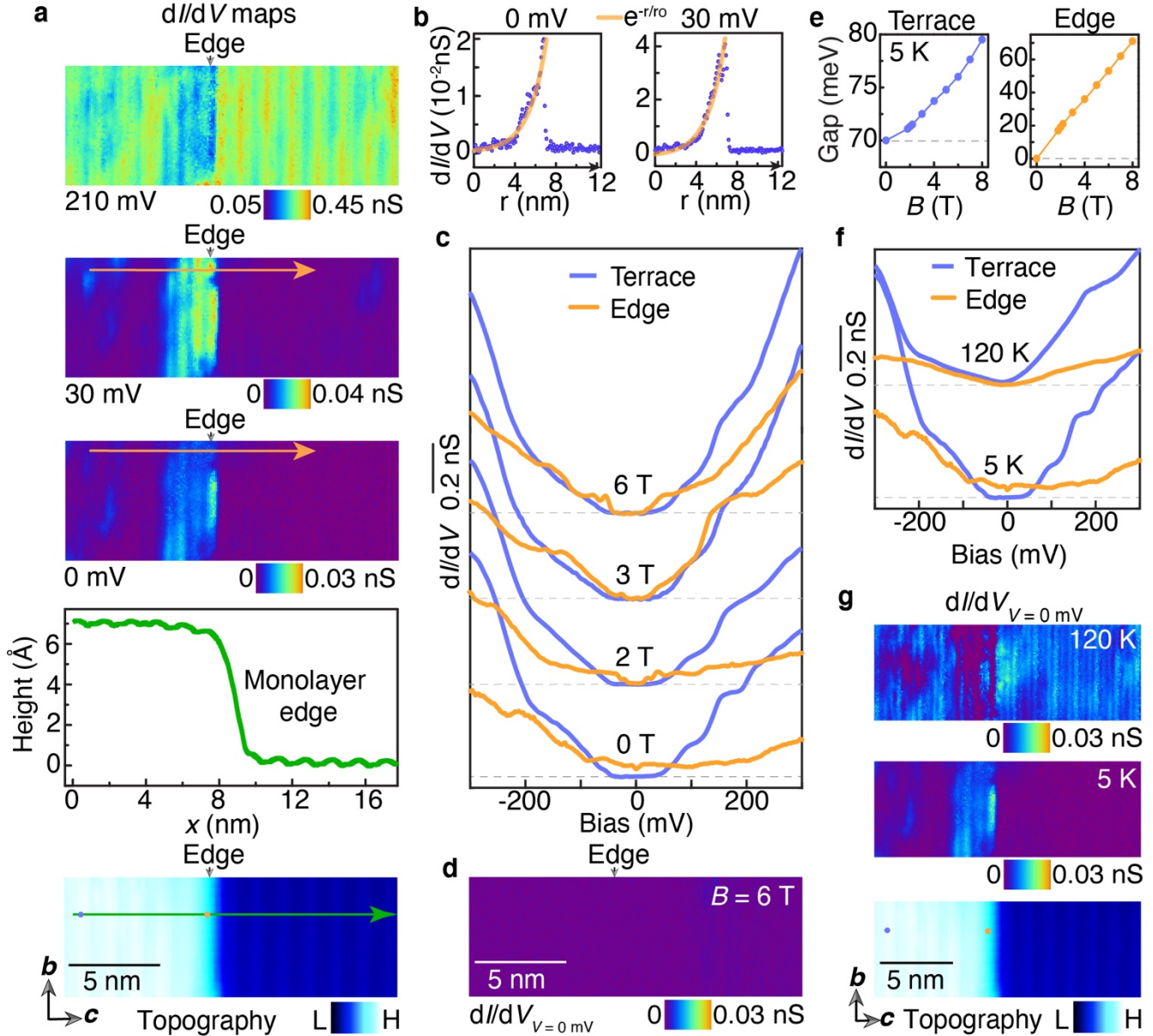


**Fig. 3: Topological nature of the insulating gap.** **a**,  $dI/dV$  maps acquired at different bias voltages (corresponding topography is shown in the bottom panel) around a monolayer step edge parallel to the  $b$ -axis, measured at  $T = 5$  K. The height profile taken perpendicular to the  $b$ -axis is also displayed. The  $dI/dV$  maps obtained within the energy gap ( $V = 0$  mV and  $30$  mV) reveal a pronounced edge state, whereas, at  $V = 210$  mV, the edge state is suppressed. **b**, Intensity distribution of the differential conductance around the step edge captured at  $V = 0$  mV and  $30$  mV. The corresponding location is marked with a green line on the topographic image in panel **a**, and the scan direction is indicated by an arrow. The red curve represents the exponential fitting ( $e^{-r/r_0}$ ) of the decay of the state away from the step edge, with a fitted decay length ( $r_0$ ) of  $1.6$  nm. **c**, Tunneling spectra at locations away from the step edge and on the step edge measured under various magnetic fields. The orange and violet curves represent the differential spectra taken at the step edge and away from it, respectively. The corresponding spatial locations where the spectra are acquired are indicated by the color-coded circles on the topographic image in panel **a**. Spectra at different

magnetic fields are taken at the same locations and are offset for clarity. Dashed horizontal lines mark the zero  $dI/dV$  for different fields. At  $B = 0$ , tunneling spectra reveal an energy gap around the Fermi energy away from the step edge, while a pronounced gapless, in-gap state is observed on the step edge. In contrast, at  $B = 2$  T, 3 T, and 6 T, the step edge state is suppressed, and an energy gap gradually develops with increasing magnetic field. **d**,  $dI/dV$  map at  $B = 6$  T ( $V = 0$  mV) taken in the same region as in panel **a**, exhibiting suppressed differential conductance along the edge. **e**, Measured spectroscopic energy gaps at the terrace (left) and the step edge (right) plotted as a function of magnetic field. Both energy gaps increase reasonably linearly with the magnetic field. **f**, Tunneling spectra at locations away from the step edge and on the step edge measured at temperatures  $T = 120$  K and 5 K. The orange and violet curves represent the differential spectra taken at the step edge and away from it, respectively. Spectra at the two temperatures are taken at the same locations and are offset for clarity. Dashed horizontal lines mark the zero  $dI/dV$  for different temperatures. At  $T = 120$  K, the energy gap at the terrace is nonexistent, and the spectrum at the step edge becomes suppressed (with respect to the  $dI/dV$  spectrum at the terrace) near the Fermi energy, visualizing the disappearance of the edge state. **g**,  $dI/dV$  maps at the Fermi energy ( $V = 0$  mV) around a monolayer step edge parallel to the  $b$ -axis measured at  $T = 120$  K and 5 K. The corresponding topography is shown in the bottom panel. The color-coded circles overlaid on the topographic image correspond to the specific spatial locations where the  $dI/dV$  spectra in panel **f** were acquired. The  $dI/dV$  map at  $T = 5$  K shows a pronounced edge state, whereas at  $T = 120$  K, the edge state is suppressed, indicating a direct correspondence between the emergence of the gapped bulk exciton insulator state and the gapless edge state. Tunneling junction set-up:  $V_{\text{set}} = 300$  mV,  $I_{\text{set}} = 0.5$  nA,  $V_{\text{mod}} = 2$  mV.

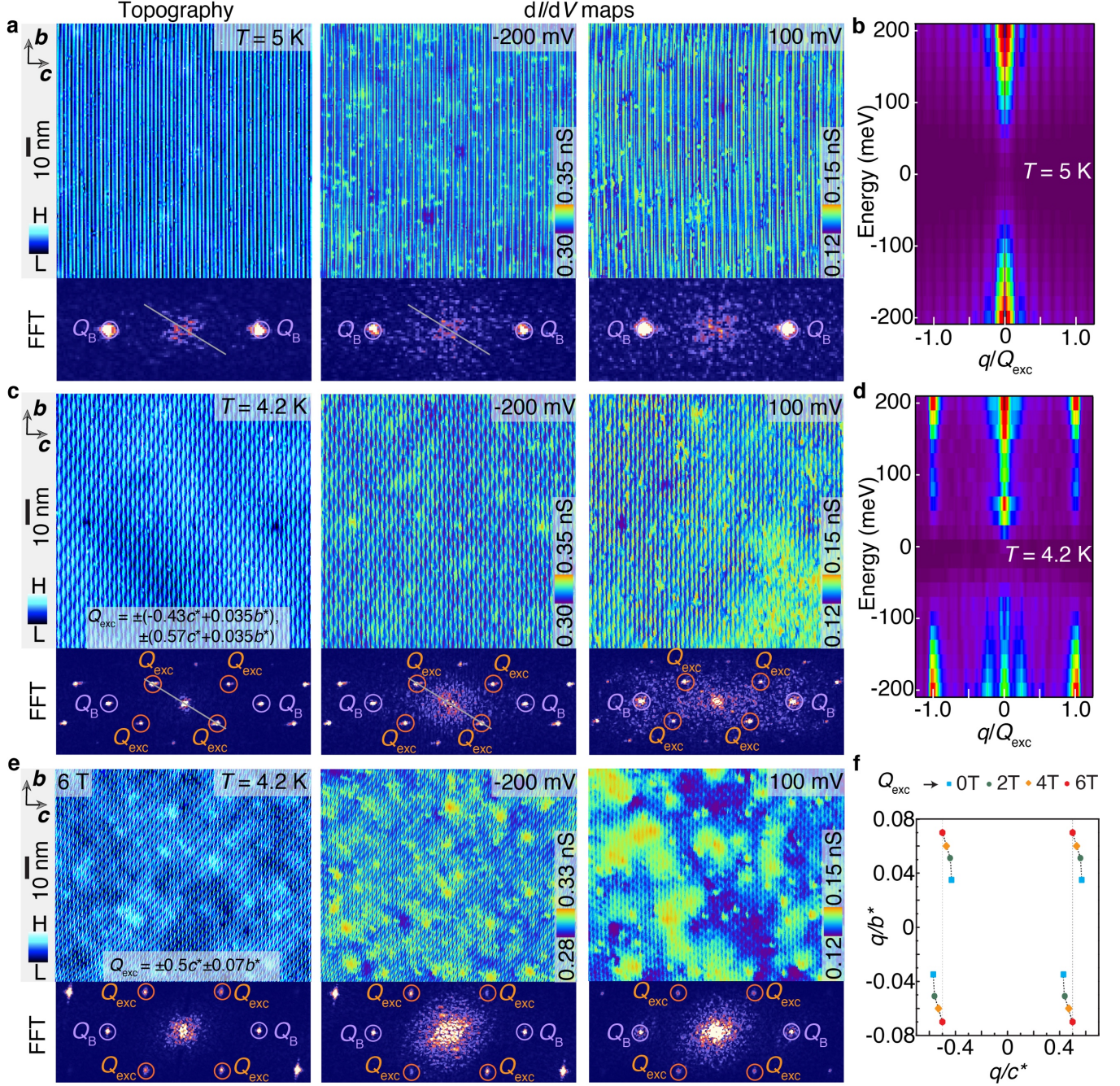


**Fig. 4: Observation of a secondary exciton instability with non-zero wavevector and translation symmetry breaking.** **a**, Topography (left panel) and  $dI/dV$  maps acquired at the occupied ( $V = -200$  mV) and unoccupied side ( $V = 100$  mV) of the insulating gap measured at  $T = 5$  K. The bottom panels show the corresponding Fourier transform images revealing well-developed Bragg peaks (purple circles). **b**, Energy dependence of the Fourier transform magnitude along the line cut marked with a grey line in the Fourier transform images (the horizontal axis is normalized by  $Q_{\text{exc}}$ , defined in panel c). **c**, Topography (left panel) and  $dI/dV$  maps acquired at the occupied ( $V = -200$  mV) and unoccupied side ( $V = 100$  mV) of the insulating gap, measured at  $T = 4.2$  K, showing a pronounced translation symmetry breaking order revealed through topographic and spectroscopic contrast. Notably,

there is a spectroscopic contrast reversal when the bias is switched between the occupied and unoccupied sides of the insulating gap. The Fourier transform images of the topography and the  $dI/dV$  maps shown on the bottom panels display well-defined wavevector peaks (orange circles) alongside the Bragg peaks (green circles). The wavevector,  $Q_{\text{exc}} = \pm(-0.43c^* + 0.035b^*), \pm(0.57c^* + 0.035b^*)$ . **d**, Energy-dependent Fourier transform magnitude along the linecut indicated with a grey line in the Fourier transform images showing the energy dependence of  $Q_{\text{exc}}$ ; the linecut position is the same as in panel **a**. Akin to panel **b** data, the horizontal axis here is also normalized by  $Q_{\text{exc}}$ . In contrast to panel **b** data, however, here, non-dispersing, well-developed peak intensity is seen at  $q = Q_{\text{exc}}$  on both sides of the insulating energy gap. **e**, Topography (left panel) and  $dI/dV$  maps acquired at the occupied ( $V = -200$  mV) and unoccupied side ( $V = 100$  mV) of the energy gap, measured at  $T = 4.2$  K under an external magnetic field of 6 T, revealing the topographic and spectroscopic contrast associated to the translation symmetry breaking order. Akin to panel **c**, there is a spectroscopic contrast reversal when the bias is switched between the occupied and unoccupied sides of the insulating gap. The Fourier transform images of the topography and the  $dI/dV$  maps shown on the bottom panels display well-defined wavevector peaks (orange circles) alongside the Bragg peaks (purple circles). Strikingly, here  $Q_{\text{exc}} = \pm(0.5c^* + 0.07b^*)$  is different from the  $Q_{\text{exc}}$  at zero magnetic field. **f**, Scatter plot highlighting the magnetic field tunability of  $Q_{\text{exc}}$ . Starting from being incommensurate along both  $b$  and  $c$  axes at  $B = 0$  T, the wavevector  $Q_{\text{exc}}$  evolves gradually with increasing field and becomes commensurate along the  $c$ -axis at  $B = 6$  T. Tunneling junction set-up:  $V_{\text{set}} = 300$  mV,  $I_{\text{set}} = 0.5$  nA,  $V_{\text{mod}} = 2$  mV.

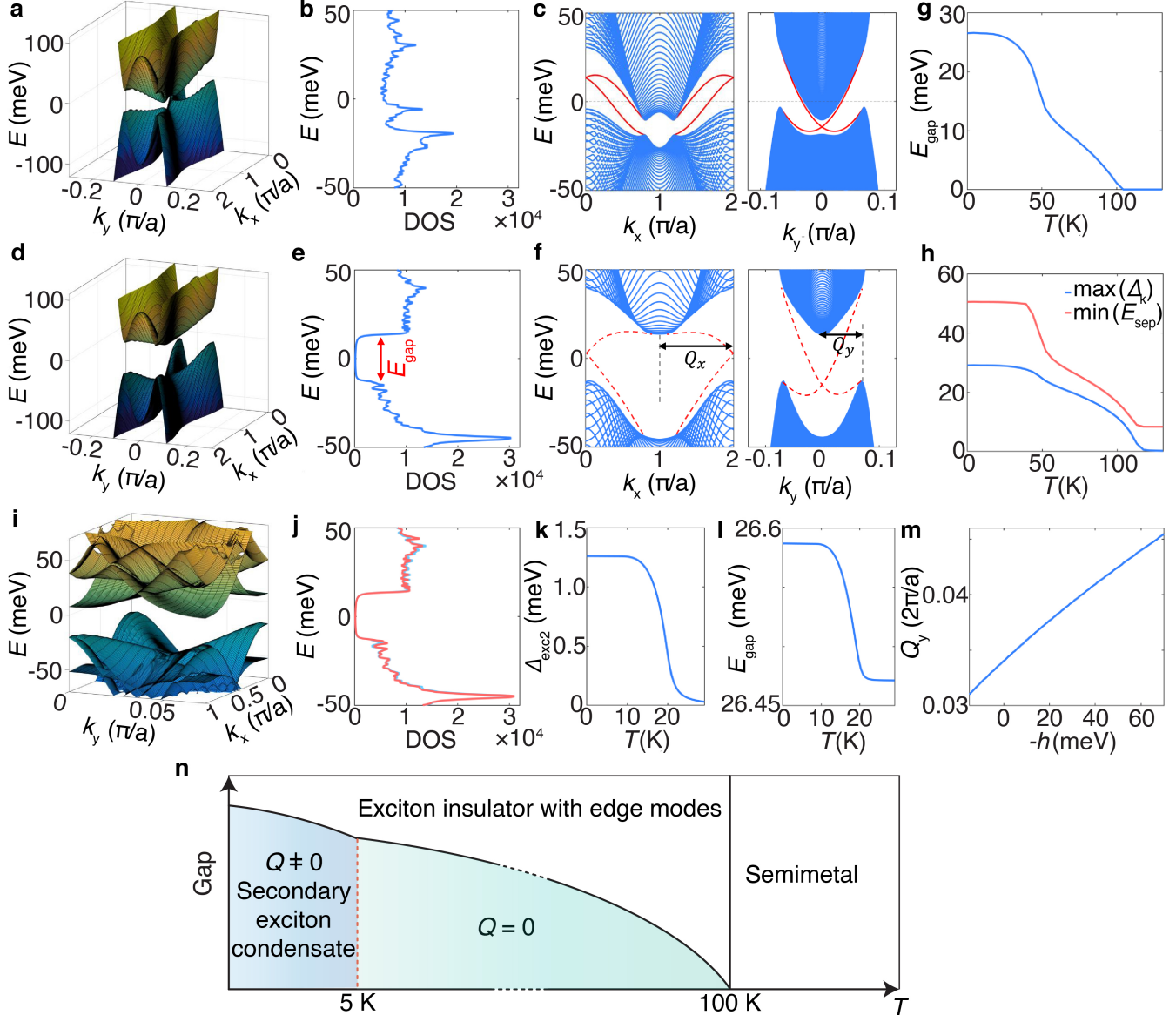


**Fig. 5: Theoretical modelling of the primary and secondary exciton condensation transition.** **a**, Low-energy band structure in the absence of excitonic phase. **b**, Density of states in the absence of the excitonic phase. The system is metallic with the conduction band minimum located at 6.6 meV below the valence band maximum. **c**, Band structure of a ribbon geometry with open boundaries along the  $y$ - (left) and  $x$ -directions (right), respectively. The blue bands represent the bulk continuum. The red curves illustrate the edge states that connect the conduction and valence bands. **d**, Band structure in the presence of a primary excitonic order at  $T = 10^{-3}$  K and  $V_0 = 1.25$  eV. **e**, Density of states in the presence of the primary excitonic order, exhibiting the opening of a fully developed bulk gap  $E_{\text{gap}} \approx 26.5$  meV. **f**, Projection of the band structure into the  $x$ - (left) and  $y$ -directions, respectively. The red dashed curves indicate the edge states.  $Q_x$  and  $Q_y$  denote the momentum separation between the conduction band minimum and valence band maximum in the  $k_x$ - and  $k_y$ -directions, respectively. **g**, Band energy gap  $E_{\text{gap}}$ , plotted as a function of temperature  $T$ , exhibiting a monotonic decrease with the increase of  $T$  and an entire disappearance for  $T \geq 100$  K, reminiscent of our experimental observation. According to our mean-field self-consistent simulation, the change of slope near  $T = 50$  K stems from the fact that the Fermi energy crosses only



the conductance band. When the Fermi energy is between the conductance and valence (or crosses both the conductance and valence band), the change of slope disappears. **h**, Maximum value of the primary excitonic order parameter in the momentum space  $\max(\Delta_{\mathbf{k}})$  (blue curve) and minimum separation of the conduction and valence bands  $\min(E_{\text{sep}})$  (red curve) plotted against  $T$ .  $\min(E_{\text{sep}})$  is away finite when changing the temperature. **i**, Low-energy band structure in the reduced Brillouin zone (i.e.,  $k_x \in [0, Q_x]$  and  $k_y \in [0, Q_y]$ ) with both primary and secondary excitonic orders present at  $T = 10^{-3}$  K. **j**, Density of states in the presence of primary and secondary excitonic orders. We consider a slightly larger Coulomb interaction strength  $V = 1.02V_0$  for illustration. **k**, Secondary, finite momentum excitonic order parameter as a function of  $T$ , which develops below 20 K. **l**, Evolution of the bulk energy gap  $E_{\text{gap}}$  with  $T$ . The secondary exciton order slightly augments  $E_{\text{gap}}$ . **m**, Momentum separation of the valence band maximum and the  $\Gamma$  point,  $Q_y$ , shown as a function of the Zeeman-like energy  $h$ . **n**, A schematic phase diagram of the discovered phases in  $\text{Ta}_2\text{Pd}_3\text{Te}_5$ .

## Methods:

### I. Single-crystal synthesis

$\text{Ta}_2\text{Pd}_3\text{Te}_5$  single crystals were synthesized using the flux method. A mixture of Ta powder (99.995% purity), Pd powder (99.95% purity), and Te chunks (99.99% purity) in a molar ratio of 2:4.5:7.5 was sealed in an evacuated quartz tube. All the manipulations were performed in an argon-filled glovebox to maintain an inert atmosphere. The sealed ampule was then heated to 950°C over a period of 10 hours and held at that temperature for 48 hours to allow for crystal growth. Subsequently, the ampule was gradually cooled to 800°C with a ramp rate of 2 K/h. At this temperature, any excess liquid was removed through a centrifuging process. The resulting  $\text{Ta}_2\text{Pd}_3\text{Te}_5$  single crystals obtained from the growth process are shiny, rod-like, and exhibit a silver-gray color.

### II. Scanning tunneling microscopy

Single crystals were cleaved mechanically in situ at  $T = 77$  K under ultra-high vacuum conditions ( $< 5 \times 10^{-10}$  mbar). Immediately after cleaving, the crystals were inserted into the microscope head, which was already at the  $^4\text{He}$  base temperature (4.2 K). More than 20 single crystals were cleaved for this study. For each cleaved crystal, we explored surface areas over  $10 \mu\text{m} \times 10 \mu\text{m}$  to search for atomic flat surfaces. Topographic images were acquired in constant current mode. Tunneling conductance spectra were obtained with a commercial Ir/Pt tip (annealed under ultra-high vacuum condition and then characterized with a reference sample) using standard lock-in amplifier techniques with a lock-in frequency of 977 Hz. The tunneling junction set-ups used in the experiments are indicated in the corresponding figure captions. The magnetic field was applied through a zero-field cooling method. To acquire field-dependent tunneling conductance measurements, the tip was first withdrawn away from the sample, and then the magnetic field was slowly ramped to the desired value. The tip was then reapproached to the sample, and spectroscopic measurements were performed at the specific magnetic field. For temperature-dependent measurements, the tip was retracted from the sample, and the temperature was raised and stabilized for 12 hours before reapproaching the tip to the sample for tunneling measurements.

### III. Scanning transmission electron microscopy

Thin lamellae were prepared by focused ion beam cutting. All samples for experiments were polished using a 2-kV gallium ion beam to minimize the surface damage caused by the high-energy ion beam. Transmission electron microscopy (TEM) imaging, atomic-resolution high-angle annular darkfield scanning transmission electron microscopy (HAADF-STEM) imaging, and atomic-level energy-dispersive X-ray spectroscopy (EDS) mapping

were performed using a Titan Cubed Themis 300 double Cs-corrected scanning/transmission electron microscope. The microscope was equipped with an extreme field emission gun source and operated at 300 kV. Additionally, a super-X energy-dispersive spectrometry system was utilized during the experiments.

#### IV. X-ray diffraction measurements

Single crystal X-ray diffraction measurements were performed using a custom-designed X-ray instrument equipped with a Xenocs Genix3D Mo K $\alpha$  (17.48 keV) X-ray source, delivering  $2.5 \times 10^7$  photons/sec in a beam spot size of 150  $\mu\text{m}$  at the sample position. The samples under investigation were mounted on a Huber 4-circle diffractometer and cooled using a closed-cycle cryostat with a beryllium dome. The diffraction signals were captured by a highly sensitive single-photon counting PILATUS3 R 1M solid-state area detector, boasting  $981 \times 1043$  pixels, each with a size of 172  $\mu\text{m} \times 172 \mu\text{m}$ . During data acquisition, images were taken in  $0.1^\circ$  increments while rotating the samples, and these images were subsequently converted into three-dimensional mappings in momentum space. The crystal structure of the samples was confirmed to conform to the space group Pnma. The lattice parameters at room temperature were determined to be  $a = 13.973 \text{ \AA}$ ,  $b = 3.7098 \text{ \AA}$ , and  $c = 18.564 \text{ \AA}$ , with a measurement system error of 0.3%.

#### V. Angle-resolved photoemission spectroscopy

Synchrotron-based angle-resolved photoemission spectroscopy (ARPES) measurements were performed on single crystals, cleaved in ultra-high vacuum ( $< 5 \times 10^{-10}$  mbar) on the ARPES manipulator. Unless otherwise stated, the impinging light was p-polarized with an energy of 50 eV and the sample geometry was such that the  $\bar{\Gamma} - \bar{Z}$  direction lay within the scattering plane. High-resolution energy/moment slices and energy distribution curves presented in Fig. 1 were collected at beamline 4 of the Advanced Light Source (ALS) in Berkeley, USA. Polar maps shown in Extended Fig. 5 were also collected at the ALS. The polarization-dependent data in Fig. 2 were collected at the LOREA beamline at ALBA synchrotron in Barcelona, Spain. Deflection measurements in Extended Fig. 5 were taken at the National Synchrotron Light Source in Brookhaven, USA.

#### VI. First-principles calculations

Electronic structure calculations were performed within the density functional theory framework using the Vienna Ab initio Simulation Package (VASP)<sup>54,55</sup>. The General gradient approximation functional is used for treating the exchange-correlation effect<sup>56</sup>. The relativistic effect of spin-orbit coupling was included self consistently in the calculations. An energy tolerance of  $10^{-6}$  eV was used. We have performed the calculations using  $4 \times 8 \times 4$  k-mesh centered at the  $\Gamma$ -point for Bulk, and  $1 \times 8 \times 4$  k-mesh for monolayer. We extracted the real space tight-binding Hamiltonian by Wannier function using the Wannier90 code<sup>57</sup> with  $d$ -orbitals of Ta and Pd, and  $p$ -orbitals of Te as projections. The Wannier tight binding Hamiltonian was used to study the topological properties using the Wannier tools package<sup>58</sup>.

#### VII. Electrical transport measurements

To fabricate the Ta<sub>2</sub>Pd<sub>3</sub>Te<sub>5</sub> sample for transport measurements, we employed a polydimethylsiloxane (PDMS) stamp-based mechanical exfoliation technique. First, we patterned the sample contacts on the silicon substrates with a 280 nm layer of thermal oxide using electron beam lithography, followed by chemical development and metal deposition (5 nm Cr/35 nm Au). The fresh Ta<sub>2</sub>Pd<sub>3</sub>Te<sub>5</sub> flakes were mechanically exfoliated from bulk single crystals on PDMS stamps. We carefully selected thick flakes (to capture the bulk properties of Ta<sub>2</sub>Pd<sub>3</sub>Te<sub>5</sub>) with good geometry through optical microscopy. Next, we transferred the flakes onto the SiO<sub>2</sub>/Si substrates that had pre-patterned Cr/Au electrodes in place. To preserve the intrinsic properties of the compound and minimize

environmental effects, we encapsulated the samples using thin polymethyl methacrylate films with thicknesses around  $\sim 50$  nm, which ensured that the samples on the devices were never exposed to air directly. All sample fabrication processes were performed in a glovebox equipped with a gas purification system ( $<1$  ppm of  $O_2$  and  $H_2O$ ).

Electrical transport measurements were conducted using an Oxford Heliox system with a temperature range of 0.3 K to 8 T. We employed a standard four-probe method to measure the resistance and differential resistance of the sample, utilizing a lock-in amplifier technique with a lock-in frequency of 13 Hz. The reproducibility of the results was confirmed by conducting measurements in the National High Magnetic Field Laboratory in Tallahassee, Florida, USA. To ensure consistency, multiple devices were prepared and measured over multiple runs.

### VIII. Absence of structural phase transition in $Ta_2Pd_3Te_5$

As the presence of a structural phase transition can complicate the experimental detection of the transition to the excitonic insulator state, it is crucial to investigate whether the observed excitonic insulator transition in  $Ta_2Pd_3Te_5$  is accompanied by any structural changes. For this purpose, we conducted a detailed structural analysis utilizing transmission electron microscopy. Our scanning transmission electron microscopy data reveals consistent atom arrangements compared to the pristine  $Ta_2Pd_3Te_5$  crystal structure on different surfaces (Extended Fig. 1a,c and Extended Fig. 2). Importantly, the selected area electron diffraction patterns obtained from the focused-ion-beam cut lamella at  $T = 290$  K and 90 K exhibit identical crystal symmetry at both temperatures (Extended Fig. 1b,d). This observation provides compelling evidence that no structural phase transition takes place within this temperature range, indicating that the transition to the exciton insulator state near  $T = 100$  K is not accompanied by any structural changes.

We have conducted X-ray diffraction measurements at different temperatures (ranging from  $T = 300$  K to 20 K) to strengthen our conclusion regarding the absence of a structural phase transition in  $Ta_2Pd_3Te_5$ . The results are summarized in Extended Fig. 3. Analysis of the diffraction patterns collected at various temperatures reveals no additional peak emerging at low temperatures. Moreover, the data closely matches the expected Pnma structure across the entire temperature range. This consistent behavior provides crucial evidence supporting the absence of a structural phase transition within the measured temperature range. Hence, we attribute the transition to the insulating state near 100 K solely to exciton condensation.

### IX. Energy gap determination from the tunneling spectra

In this section, we present a procedure that we utilize to determine the value of the spectroscopic energy gap from  $dI/dV$  curves. The key idea is to identify the edges of the energy gap, where a discernible non-zero  $dI/dV$  signal can be distinguished from the noisy zero  $dI/dV$  signal within the gap region of the curve<sup>59</sup>. The following steps outline our approach to determining the energy gap from a single  $dI/dV$  curve (refer to Extended Fig. 4):

1. Initially, we select a bias range where the  $dI/dV$  signal takes the form:  $dI/dV = 0 + \xi$ , where 0 represents the mean  $dI/dV$  value within the spectroscopic gap and  $\xi$  represents the noise in the  $dI/dV$  signal. This is done for a bias voltage range  $V \in [V_1, V_2]$ , while avoiding the edges of the spectroscopic gap.
2. Next, we calculate the standard deviation of the noisy  $dI/dV$  signal within the gap, denoted as  $\sigma = \sqrt{\xi^2}$ . By determining  $\sigma$  from the gap segment of the  $dI/dV$  curve, we establish a noise floor for the  $dI/dV$  signal.
3. We assume a Gaussian distribution of  $\xi$  and define  $\Gamma = 2.36\sigma$ , which represents the full width at half maximum. Two Gaussian signals can be distinguished if the difference between the means of the signals is

greater than the full width at half maximum. Thus, we set  $\Gamma$  as the instrumental resolution of the  $dI/dV$  signal.

4. A non-zero  $dI/dV$  signal can only be detected when  $dI/dV > \Gamma$  with our instrumental resolution. We set  $\Gamma$  as a threshold value for identifying the edges of the energy gap.
5. By solving the equation  $dI/dV = \Gamma$ , we determine the intersections  $V_a, V_b$  of the threshold value with the  $dI/dV$  spectroscopic curve.  $eV_a$  and  $eV_b$  represent the energies of the gap edge above and below  $E_F$ , respectively. Finally, we calculate  $\Delta = eV_a - eV_b$  to obtain the value of the spectroscopic energy gap.

## X. Photoemission matrix element effect

We acquired a  $k_{\parallel}$  vs.  $k_{\perp}$  vs. E angle-resolved photoemission spectroscopy map over a wide range of angles to capture multiple Brillouin zones. Upon tuning the energy to 600 meV below the Fermi level, we observe a significant deviation from periodic structure from one Brillouin zone to the next (Extended Fig. 5a). This is likely due to sublattice interference effects since band unfolding is also present in the deflection-based map that maintains the fixed sample orientation throughout the measurement (Extended Fig 5b)<sup>60</sup>. Focusing our analysis on the vicinity of the  $\Gamma$  point of each Brillouin zone, where the bands may cross the Fermi energy, we identify a significant difference between spectra in the zeroth and second Brillouin zone (Extended Fig 5c). The  $\Gamma_0$  spectrum appears to be gapped, consistent with the previous photoemission studies<sup>30,60</sup>, while the  $\Gamma_2$  spectrum clearly displays states on the Fermi surface, in agreement with the high-temperature (semi)metallicity of Ta<sub>2</sub>Pd<sub>3</sub>Te<sub>5</sub>. Furthermore, by examining photoemission energy vs. momentum cuts perpendicular to the analyzer slit, we confirm that the spectrum appears gapped until the second Brillouin zone is reached, at which point the bands extending across the Fermi level exhibits strong spectral weight (Extended Fig 5d).

## XI. Extended scanning tunneling microscopy results on the edge states

The existence of edge states in Ta<sub>2</sub>Pd<sub>3</sub>Te<sub>5</sub> was reported in a previous work. In our study, presented in Fig. 3, we take a crucial step beyond the observation of the edge state by providing compelling evidence for its exponential localization and time-reversal-symmetry-protected,  $Z_2$  topological nature. In this section, we further support the data presented in Fig. 3 by providing extended results on the time-reversal-symmetry-protected nature of the edge state along different edge configurations. Extended Fig. 6 summarizes our scanning tunneling microscopy measurements on two types of atomic step edges: (i) a monolayer step edge running along the  $c$ -axis, perpendicular to the one-dimensional Te chains, and (ii) a four-atomic-layer thick step edge along the  $b$ -axis.

In Extended Fig. 6a, we show a monolayer atomic step edge along the  $c$ -axis, identified through the topographic image and corresponding height profile. Notably, the spatially resolved  $dI/dV$  map at the Fermi energy, within the insulating bulk gap, reveals a pronounced edge state, akin to the presence of the edge state in the step edge along the  $b$ -axis shown in Fig. 3a. Energy-resolved  $dI/dV$  spectra on the step edge (Extended Fig. 6b) exhibit a substantial  $dI/dV$  signal (orange curves) around the Fermi energy, while the  $dI/dV$  spectrum away from the step edge (violet curves) displays an insulating gap. Additionally, akin to the monolayer step edge along the  $b$ -axis, the application of an external magnetic field perpendicular to the  $bc$  plane leads to significant suppression of the  $dI/dV$  measured at the step edge. The field-dependent tunneling spectra, shown for  $B = 0$  T, 2 T, and 4 T in Extended Fig. 6b, demonstrate a gradual formation of an insulating gap at the edge state spectrum, confirming its time-reversal symmetry protected nature. The presence of the edge state and its time-reversal symmetry protected nature is also observed in multilayer step edges. For instance, we present topography, corresponding height profile, and spectroscopic measurements on a four-atomic-layer thick step edge in Extended Figs. 6c and 6d. The spectroscopic

mapping reveals a pronounced gapless in-gap state at the Fermi energy at  $B = 0$ , while the tunneling spectra at  $B = 0$  T, 2 T, and 4 T exhibit a progressively developing energy gap with an increasing magnetic field, highlighting the presence of a time-reversal-symmetry-protected, topological edge state in the four-layer step edge.

## **XII. Extended scanning tunneling microscopy data on the field tunability of the secondary translation symmetry breaking excitonic order**

Here, we present high-resolution topographic images obtained through scanning tunneling microscopy, revealing the translation symmetry breaking ordering in  $\text{Ta}_2\text{Pd}_3\text{Te}_5$ . In Extended Fig. 7a, we display an atomically resolved topographic image of a pristine  $\text{Ta}_2\text{Pd}_3\text{Te}_5$  (100) surface acquired at  $T = 5$  K. The inset shows the corresponding Fourier transform image, indicating Bragg peaks along the  $c$ -axis. It is worth noting that we are focusing on a small region in the Fourier transform image, and the Bragg peaks along the  $b$ -axis are located further away in  $q$ -space (refer to Fig. 1). At  $T = 5$  K, no wavevector peaks are visible. However, when the sample is cooled to  $T = 4.2$  K, within the same region as in Extended Fig. 7a, we observe clear translation symmetry breaking in real space (Extended Fig. 7b). The corresponding Fourier transform image, plotted in the same range as the inset in Extended Fig. 7a, now exhibits distinct superlattice peaks labeled as  $Q_{\text{exc}}$ .

Having observed the emergence of the translation symmetry breaking superlattice order at  $T = 4.2$  K, we proceed to investigate its magnetic field dependence. In Extended Fig. 7c-e, we present topographic images captured under magnetic fields of 2 T, 4 T, and 6 T, respectively. The topographic images clearly demonstrate the evolution of the superlattice modulation pattern as the magnetic field changes. This evolution is further highlighted in the corresponding Fourier transform images, all plotted within the same  $q$  range, which illustrate the variation of  $Q_{\text{exc}}$  with increasing magnetic field. Notably, the positions of the Bragg peaks ( $Q_{\text{B}}$ ) remain unaffected by the magnetic field, as expected. To quantitatively summarize the change in  $Q_{\text{exc}}$  as a function of the magnetic field, Extended Fig. 7f displays a polar plot of the vector,  $Q_{\text{exc}}$  at various magnetic field strengths (a scatter plot for  $Q_{\text{exc}}$  at different magnetic fields is shown in Fig. 4f). The plot clearly demonstrates the gradual evolution of  $Q_{\text{exc}}$  with increasing magnetic field, in accordance with the behavior expected for a finite momentum exciton condensate. This behavior may arise due to the Zeeman effect experienced by the particle and hole bands associated with the exciton condensate upon the application of a magnetic field. The resulting Zeeman shift in the bands causes a change in the exciton wavevector, which manifests in real space through the variation of  $Q_{\text{exc}}$ .

## **XIII. Transport evidence of the translation symmetry breaking secondary excitonic order and its field tunability**

In this section, we present electrical transport evidence to support the formation of a translation symmetry breaking order, indicating that it is a bulk phenomenon rather than a surface effect.

To conduct systematic electrical transport measurements, we fabricated four-point probe devices (as shown in Extended Fig. 8a) using mechanically exfoliated flakes that are thick enough to capture the bulk properties of  $\text{Ta}_2\text{Pd}_3\text{Te}_5$ . The sample resistance as a function of temperature is displayed in Extended Fig. 8b. The left inset of Extended Fig. 8b highlights a slight decrease in resistance with temperature until around  $T \simeq 100$  K, indicating a semimetallic behavior. However, below  $T \simeq 100$  K, the resistance starts to increase rapidly as the temperature decreases, exhibiting insulating behavior. Additionally, a small kink in the resistance is observed near  $T \simeq 5$  K (right inset of Extended Fig. 8b).

To investigate the translation symmetry breaking order, we explore the motion of this order under a DC electric field. The translation symmetry breaking order is expected to be pinned by the ubiquitous disorder potential created by impurities but can be de-pinned<sup>62</sup> under a sufficiently large electric field causing the order to slide. Therefore, the current-voltage characteristics should exhibit non-linear behavior indicative of a sliding phason mode<sup>62-64</sup>. To explore this possibility, we applied a DC current between the source and drain probes and measured the sample's differential resistance ( $dV/dI$ ) using a standard lock-in technique. We also measured the DC voltage across the voltage probes and extracted the electric field using  $E = V/L$  ( $L$  is the distance between the voltage probes). The measured threshold voltage ( $V_{\text{th}}$ ) is found to have a linear relationship with  $L$  (top inset of Extended Fig. 8d), justifying the use of  $E = V/L$  relationship. Extended Fig. 8c shows a plot of  $dV/dI$  as a function of  $E$  at various temperatures. At small values of  $E$ ,  $dV/dI$  remains constant for all temperatures. However, below  $T = 5.1$  K,  $dV/dI$  sharply decreases above a threshold electric field ( $E_{\text{th}}$ ), indicating the onset of collective phason current<sup>53</sup>. The temperature dependence of  $E_{\text{th}}$ , defined as the onset of the sharp decrease in  $dV/dI$  with respect to  $E$ , is illustrated in Extended Fig. 8d. We find that  $E_{\text{th}}$  disappears above  $T = 5.1$  K, which we identify as the transition temperature ( $T_{\text{exc2}}$ ) of the translation symmetry breaking order.

Additionally, it is crucial to consider the impact of local Joule heating on the observed transport properties. If heat were dissipated in the sample, leading to a localized temperature increase above  $T_{\text{exc2}}$ , it could potentially induce a thermally driven switching effect and result in non-linear transport characteristics. However, in such a scenario, the required dissipated power for switching would tend to approach zero as  $T$  approaches  $T_{\text{exc2}}$  from below. Contrary to this expectation, the electrical power  $P_{\text{th}} = V_{\text{th}}^2/[dV/dI(V_{\text{th}})]$  obtained at  $V_{\text{th}}$  from our experiments does not approach zero as  $T$  approaches  $T_{\text{exc2}}$  (bottom inset of Extended Fig. 8d). Instead,  $P_{\text{th}}$  decreases with decreasing temperature, which is precisely the opposite of what we would anticipate in a thermally driven switching scenario. Furthermore, it is important to note that the power dissipated in the sample, which is less than 1 pW, is significantly smaller than the cooling power of the cryostat. Moreover, the observed linear dependence of  $V_{\text{th}}$  on the distance between the voltage probes (top inset of Extended Fig. 8d) suggests that the observed characteristics are not attributed to contact effects. Instead, these observations provide compelling evidence for the presence of a propagating, current-carrying translation symmetry breaking order.

Having discussed the transport signature of the translation symmetry breaking order, we proceed to investigate how its properties evolve with the magnetic field. In Extended Fig. 8e, we present  $dV/dI$  as a function of  $E$  at various magnetic fields, applied perpendicular to the sample plane, ranging from -3 T to 7 T. The plot clearly exhibits a change in  $E_{\text{th}}$  as a function of the magnetic field. This change is further quantified in Extended Fig. 8f, which demonstrates an increase in  $E_{\text{th}}$  with an increasing magnetic field. The magnetic field-dependent behavior of the translation symmetry breaking order aligns with our scanning tunneling microscopy observations (Fig. 4 and Extended Fig. 7), where we observe a gradual change in  $Q_{\text{exc}}$  with increasing field. Notably, at  $B = 0$ , the translation symmetry breaking order is incommensurate and therefore not pinned to the lattice, explaining the small  $E_{\text{th}}$  required to de-pin the translation symmetry breaking order from the pinning potential solely contributed by the impurities. Conversely, at  $B = 6$  T, the translation symmetry breaking order becomes commensurate along one axis in the cleaving plane (the  $c$ -axis), potentially making it more difficult to de-pin the translation symmetry breaking order and requiring a larger  $E_{\text{th}}$ , consistent with our observations in Extended Fig. 8f. It is important to note that even though the translation symmetry breaking order becomes commensurate along the  $c$ -axis at  $B = 6$  T, it may or may not be directly pinned to the lattice in that direction. Overall, our electrical transport experiments, demonstrating a well-defined  $E_{\text{th}}$  that is consistent with the presence of the translation symmetry breaking order and its temperature

onset that agrees with the scanning tunneling microscopy observations, serve as bulk evidence for the existence of the bulk translation symmetry breaking order in Ta<sub>2</sub>Pd<sub>3</sub>Te<sub>5</sub> below  $T \simeq 5$  K.

#### XIV. Theoretical description of the two excitonic instabilities in Ta<sub>2</sub>Pd<sub>3</sub>Te<sub>5</sub>

The low-energy band structure of monolayer Ta<sub>2</sub>Pd<sub>3</sub>Te<sub>5</sub>, derived from first-principles calculations, is displayed in Extended Fig. 9. The conduction band minimum is situated at  $\mathbf{k} = \left(0, \frac{\pi}{c}\right)$ , while the valence band maxima are located close to the  $k_y = 0$  line. Notably, the system is gapless in the absence of excitonic order. Specifically, the bottom of the conduction band minimum is situated slightly lower (by 7 meV) than the top of the valence band maxima. Moreover, the band structure is topological and can be characterized by a nonzero topological invariant. Based on these properties, we constructed a two-band minimum model on a square lattice as follows:

$$H = \sum_{\mathbf{k}} \Psi_{\mathbf{k}}^\dagger \{ \mathcal{M}(\mathbf{k})\sigma_z + A_x \sin k_x \sigma_x + A_y \sin k_y \sigma_y + h(\mathbf{k})\sigma_0 \} \Psi_{\mathbf{k}}. \quad (1)$$

In Eq. (1),  $\Psi_{\mathbf{k}} = (c_{\alpha,\mathbf{k}}, c_{\beta,\mathbf{k}})^T$ ,  $\mathcal{M}(\mathbf{k}) = M_0 + M_x(1 - \cos k_x) + M_y(1 - \cos k_y)$ , and  $h(\mathbf{k}) = C_x(1 + \cos k_x) + C_y(1 - \cos k_y)$ .  $\{\sigma_x, \sigma_y, \sigma_z\}$  and  $\sigma_0$  are Pauli and identity matrices for pseudo-spin  $\{\alpha, \beta\}$ , and the lattice constants are set to be unity. The two energy bands are given by

$$\varepsilon_{c/v}(\mathbf{k}) = h(\mathbf{k}) \pm E(\mathbf{k}), \quad (2)$$

where  $E(\mathbf{k}) = [\mathcal{M}(\mathbf{k})^2 + A_x^2 \sin^2 k_x + A_y^2 \sin^2 k_y]^{\frac{1}{2}}$ . To mimic the low-energy band structure of monolayer Ta<sub>2</sub>Pd<sub>3</sub>Te<sub>5</sub>, we chose the following parameters:  $M_0 = -0.09$  eV,  $M_y = 4$  eV,  $M_x = 0.05$  eV,  $A_x = 0.007$  eV,  $A_y = 0.08$  eV,  $C_x = 0.004$  eV, and  $C_y = -0.3$  eV. The resulting band structure is illustrated in Fig. 5a. The conduction band minimum is located slightly lower (by 6.6 meV) than the valence band maxima. As dictated by the nontrivial topological invariant, the model exhibits gapless edge states under open boundaries. However, the edge states are buried by the bulk continuum (Fig. 5c).

**Topological excitonic instability:** We consider Coulomb interaction, which in momentum space can be expressed as<sup>65</sup>:

$$H_{\text{int}} = \frac{1}{N} \sum_{\mathbf{k}, \mathbf{k}', \mathbf{q}} W(\mathbf{q}) c_{\mathbf{k}+\mathbf{q},c}^\dagger c_{\mathbf{k}'-\mathbf{q},v}^\dagger c_{\mathbf{k}',v} c_{\mathbf{k},c}, \quad (3)$$

where  $c_{\mathbf{k},c(v)}^\dagger$  and  $c_{\mathbf{k},c(v)}$  represent creation and annihilation operators for an electron with momentum  $\mathbf{k}$  at the conduction (valence) band, respectively;  $N$  is the number of  $\mathbf{k}$ -points of the Brillouin zone;  $W(\mathbf{q})$  stands for the  $q$ -resolved screened Coulomb interaction

$$W(\mathbf{q}) = \frac{U(\mathbf{q})}{1 + 2\pi\alpha|\mathbf{q}|}, \quad (4)$$

and  $U(\mathbf{q}) = \frac{V}{|\mathbf{q}|}$  denotes the unscreened Coulomb interaction which is the dominant contribution to the electron-hole attraction. We considered two-dimensional screening effect which leads to an intrinsic  $\mathbf{q}$ -dependent dielectric function of the form  $1/(1 + 2\pi\alpha|\mathbf{q}|)$ , as shown in Eq. (4)<sup>66,67</sup>.  $V$  and  $\alpha$  are model parameters. We apply the Hartree-Fock mean-field approximation (consider  $\mathbf{k}' = \mathbf{k} + \mathbf{q}$  for the decomposition in Eq. (3)) and decouple the interaction as

$$H_{\text{exc}} = \begin{pmatrix} 0 & \Delta_{\mathbf{k}} \\ \Delta_{\mathbf{k}} & 0 \end{pmatrix} \quad (5)$$

in the band basis  $(c_{k,c}, c_{k,v})$ . The momentum-dependent order parameter  $\Delta_{\mathbf{k}}$  is calculated self-consistently by

$$\Delta_{\mathbf{k}} = -\frac{1}{N} \sum_{\mathbf{k}'} W(\mathbf{k} - \mathbf{k}') \langle c_{\mathbf{k}',c}^\dagger c_{\mathbf{k}',v} \rangle, \quad (6)$$

where  $\langle \dots \rangle$  stands for the quantum statistic average. Importantly, it should be emphasized that the order parameter is solely influenced by the Fock term.

We first consider the case in which the excitonic order couples electrons and holes possessing identical momenta. Through a self-consistent computation, utilizing an interaction strength of  $V = 1.25$  eV, a small screening factor  $\alpha = 0.2$  (in units of lattice constant), and employing a  $201 \times 561$  grid within the Brillouin zone, we observe a distinctive emergence of excitonic order. This order engenders a band gap for temperatures  $T < T_c \approx 100$  K. The order parameter  $\Delta_{\mathbf{k}}$  is most pronounced near the  $k_x$  axis (i.e.,  $k_y = 0$ ) where the two bands are closest to each. With decreasing  $T$ ,  $\Delta_{\mathbf{k}}$  becomes stronger, in turn leading to a consistent increase of the bulk gap. Ultimately, for  $T \leq 30$  K, the bulk gap saturates to a large value 26.5 meV. Notably, the valence maxima relocate to  $\pm(0, 0.071\pi)$  (as depicted in Fig. 5e).

In Fig. 5h, we calculate the maximum value of the order parameter,  $\max(\Delta_{\mathbf{k}})$ , as a function of  $T$ . We find that the critical temperature for  $\Delta_{\mathbf{k}}$  is  $T'_c \approx 140$  K, which significantly exceeds  $T_c$ . This deviation is due to the negative band gap in the bared band structure (without  $\Delta_{\mathbf{k}}$ ). Additionally, Fig. 5h portrays the minimum value of the energy separation between the conduction and valence bands,  $\min(E_{\text{sep}})$ , as a function of  $T$ . Notably,  $\Delta E_{\text{min}}$  remains consistently positive throughout. This observation indicates that, as we turn on the excitonic order by decreasing temperature, the two bands still do not touch with each other. Thus, the topology of the system stays preserved.

**Excitonic translation symmetry breaking order:** In addition to the primary excitonic order, we consider an additional excitonic order with an ordering wave vector  $\mathbf{Q} \approx (\pi, 0.035\pi)$ , which allows to couple the conduction minimum and valence maxima. In the calculation, we consider  $k + q = k' + Q$  in the Hartree-Fock decomposition. We split the Brillouin zone into small rectangular pieces with an area of  $Q_x Q_y$  and consider eight pieces with the lowest energies. For simplicity, we assume an approximately constant interaction strength,  $U_{CDW} = W(\mathbf{Q})$ , between the conduction and valence bands, originating from the next-nearest-neighbor pieces in the momentum space. We consider the same  $V = 1.25$  eV and  $\alpha = 0.2$  as that used for the primary excitons. Note that the translation symmetry breaking ordering wavevector is not necessarily commensurate. The results are the same if more pieces in the Brillouin zone are considered because the finite momentum excitonic order occurs only between the pieces that are closest to the band gap. Given that the strength of the primary excitonic order is approximately constant at the lower temperature regime ( $T < 30$  K), in the calculation of the finite momentum excitonic order, we started from the band structure addressed by the primary excitonic order. The low-energy band structure in the reduced Brillouin zone (i.e.,  $k_x \in [0, Q_x]$  and  $k_y \in [0, Q_y]$ ) with both primary excitonic and finite momentum excitonic orders at  $T = 10^{-3}$  K is displayed in Fig. 5i. In Extended Fig. 10, we also show the results for varying  $V$  at  $T = 10^{-3}$  K. Notably, we observe that the finite momentum excitonic order has a critical interaction strength close to the interaction strength used for the primary excitonic order  $V_0 = 1.25$  eV.

**Magnetic field dependence:** Here we investigate the magnetic influence on the translation symmetry breaking ordering wavevector, based on the Zeeman coupling. As discussed previously, the wavevector can be determined



by the momentum separation  $Q$  of the conduction band minimum and valence band maxima in momentum space. In the model, the magnetic field  $B$  can be incorporated through a Zeeman term

$$H_{\text{Zeeman}} = h\sigma_z. \quad (7)$$

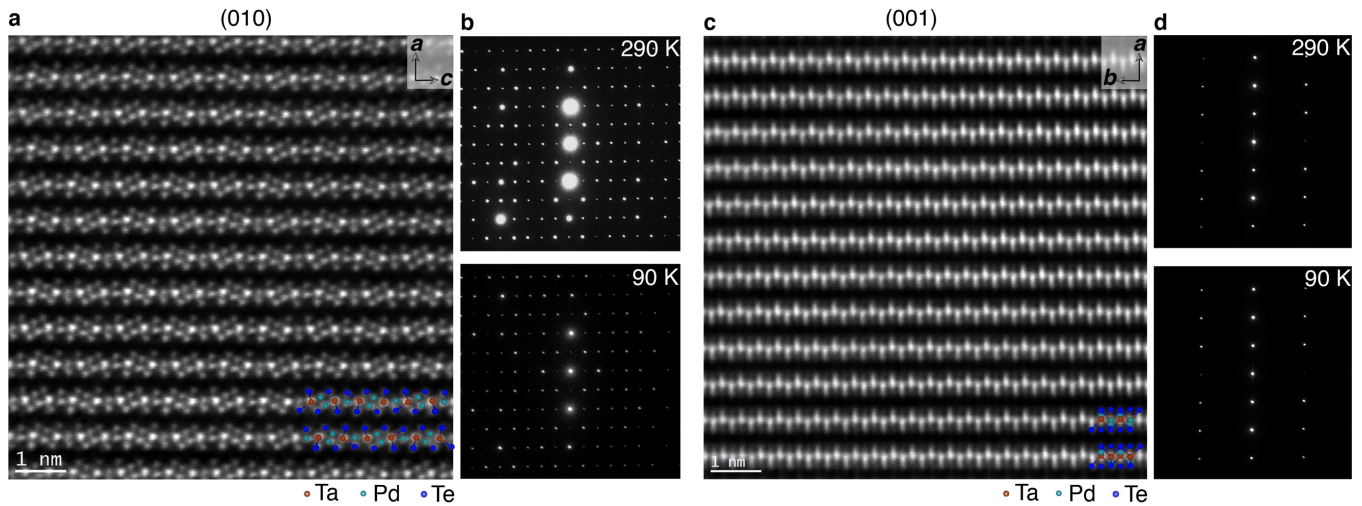
Here  $h = g\mu_B B$  represents the Zeeman energy, where  $g$  is the effective  $g$ -factor and  $\mu_B$  is the Bohr magnon. As shown before, the conduction band minimum is always located at the  $M$  point, and the  $x$ -component of  $Q$  remains relatively fixed at  $\pi$ , particularly in the presence of the primary excitonic order. Thus, it suffices to focus solely on the  $y$ -component of the translation symmetry breaking ordering wavevector. The problem can then be reformulated as the question of how  $h$  influences the  $y$ -component of the momentum separation ( $Q_y$ ), and its solution is illustrated in Fig. 5m.

Finally, it is important to emphasize that, from a broad perspective, the exciton insulator is expected to endure high magnetic fields due to the absence of a Meissner effect (seen in superconductors). Fenton<sup>71</sup> investigated the field dependence of the exciton insulator based on orbital coupling, demonstrating that in systems with band overlap (such as  $\text{Ta}_2\text{Pd}_3\text{Te}_5$ ) or in small bandgap semiconductors, the application of a magnetic field induces a stronger exciton insulator than without a field. Note that ref. <sup>71</sup> assumes isotropic bands, thus implying no anticipated shift in the wavevector. In a more complete consideration, the combination of orbital and Zeeman effects as well as Fermi surface anisotropies need to be taken into account. In materials featuring anisotropic bands like  $\text{Ta}_2\text{Pd}_3\text{Te}_5$ , this would generically also lead to a shift in the wavevector of the exciton order with applied magnetic field, in particular if the initial state is incommensurate. These basic trends – magnetic field enhancement of the exciton gap as well as a shift of the ordering wave vector – are fully consistent with our experimental observations.

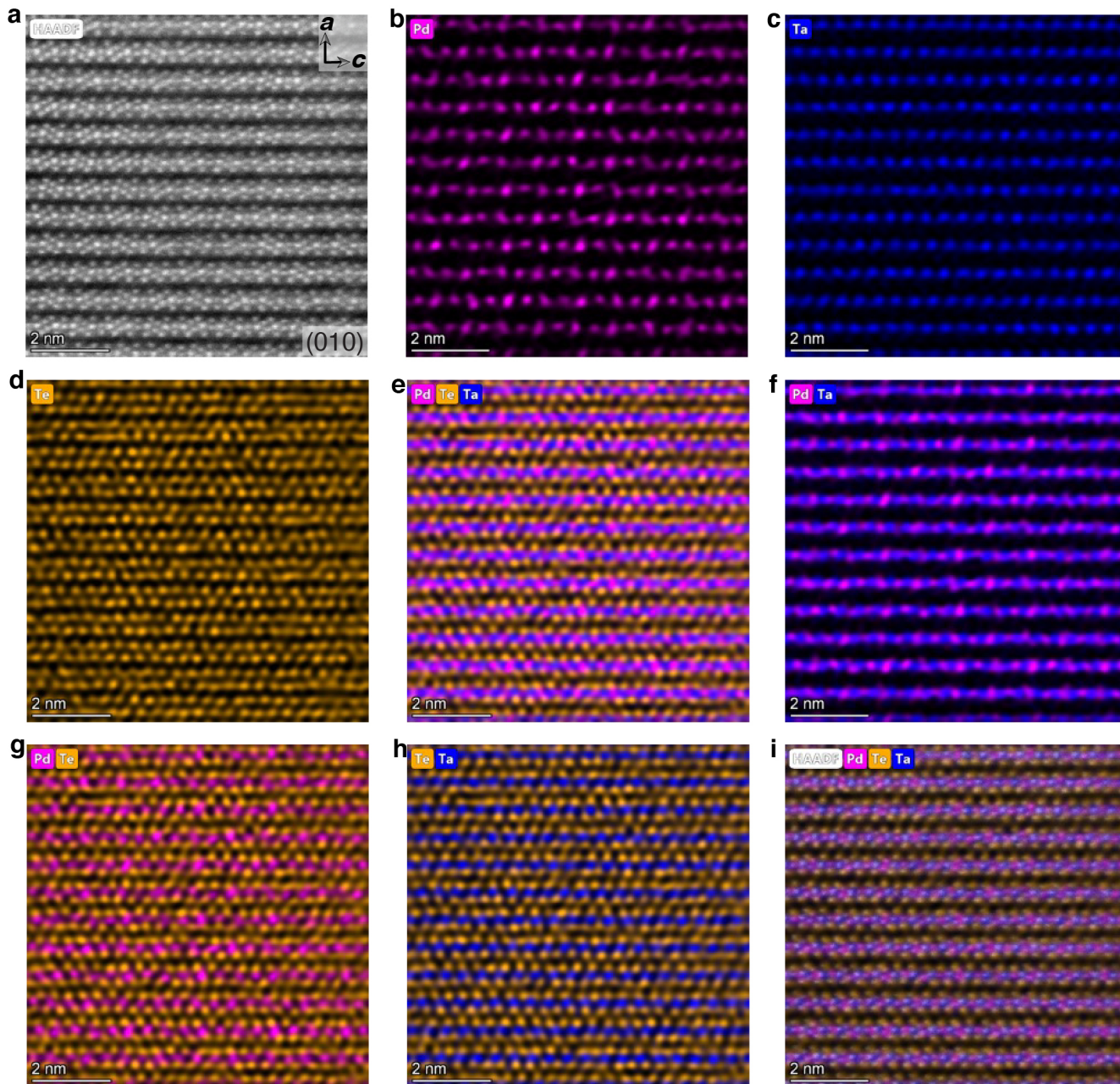
## References

54. Hohenberg, P. & Kohn, W. Inhomogeneous electron gas. *Phys. Rev.* **136**, B864 (1964).
55. Kresse, G. & Furthmüller, J. Efficient iterative schemes for ab initio total-energy calculations using a plane-wave basis set. *Phys. Rev. B* **54**, 11169 (1996).
56. Perdew, J. P., Burke, K. & Ernzerhof, M. Generalized gradient approximation made simple. *Phys. Rev. Lett.* **77**, 3865 (1996).
57. Mostofi, A., Yates, J. R., Lee, Y. -S., Souza, I., Vanderbilt, D. & Marzari, N. wannier90: A tool for obtaining maximally-localised Wannier functions. *Comput. Phys. Commun.* **178**, 685 (2008).
58. Wu, Q., Zhang, S., Song, H.-F., Troyer, M. & Soluyanov, A. A. WannierTools: An open-source software package for novel topological materials. *Comput. Phys. Commun.* **224**, 405 (2018).
59. Lee, I. et al. Imaging Dirac-mass disorder from magnetic dopant atoms in the ferromagnetic topological insulator  $\text{Cr}_x(\text{Bi}_{0.1}\text{Sb}_{0.9})_{2-x}\text{Te}_3$ . *Proc. Natl Acad. Sci.* **112** 1316-1321 (2014).
60. Cheng, Z. et al. Visualization of Tunable Weyl Line in A–A Stacking Kagome Magnets. *Adv. Mater.* **35**, 2205927 (2023).
61. Wang, A. et al. A robust and tunable Luttinger liquid in correlated edge of transition-metal second-order topological insulator  $\text{Ta}_2\text{Pd}_3\text{Te}_5$ . arXiv:2210.06685 (2022).
62. Bardeen, J. Tunneling theory of charge-density-wave depinning. *Phys. Rev. Lett.* **45**, 1978 (1980).
63. Wang, Z. Z. et al. Charge density wave transport in  $(\text{TaSe}_4)_2\text{I}$ . *Solid State Commun.* **46**, 325–328 (1983).
64. Gooth, J. et al. Axionic charge-density wave in the Weyl semimetal  $(\text{TaSe}_4)_2\text{I}$ . *Nature* **575**, 315–319 (2019).
65. Gao, Q. et al. Evidence of high-temperature exciton condensation in a two-dimensional semimetal. *Nat. Commun.* **14**, 994 (2023).

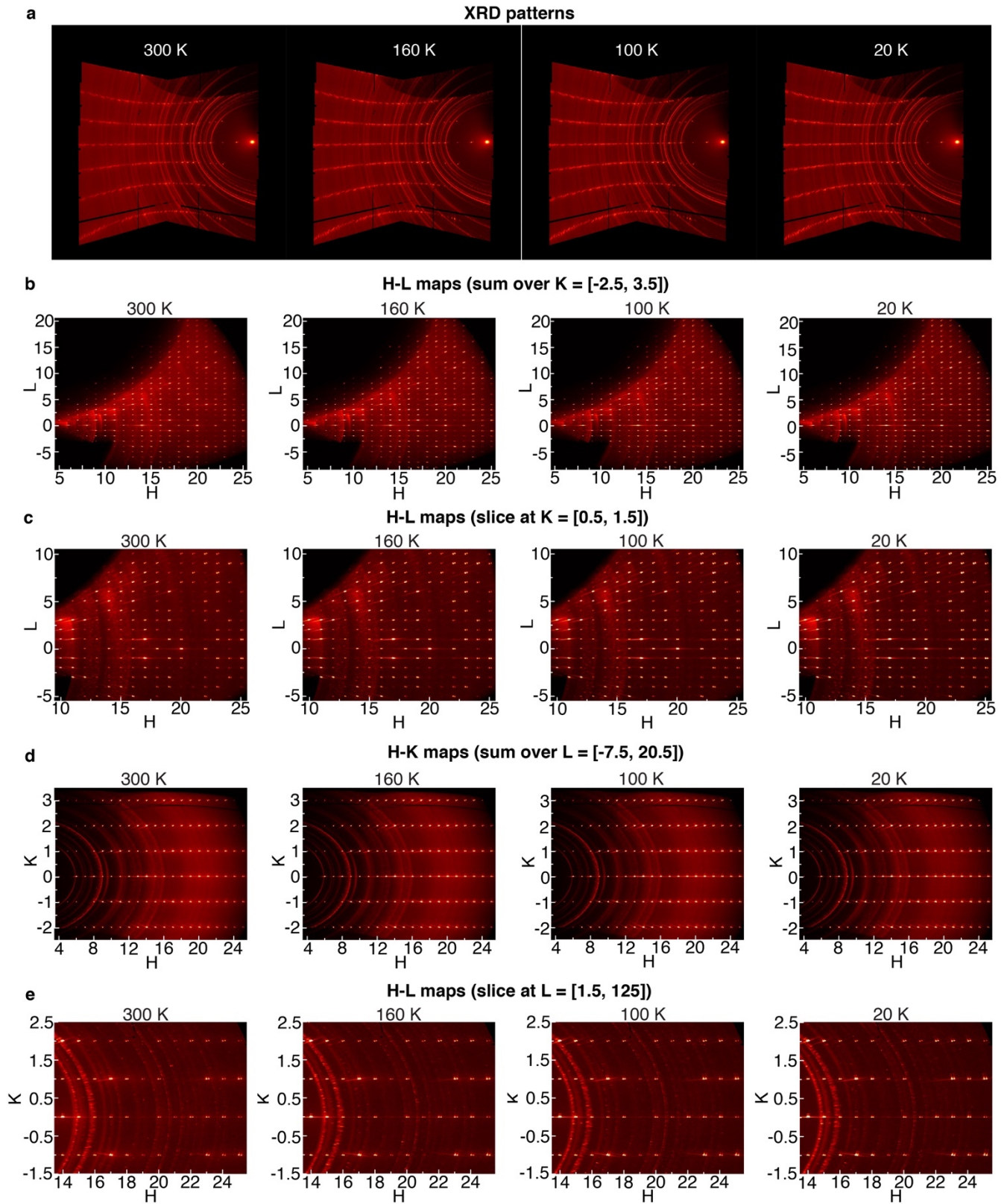
66. Cudazzo, P., Tokatly, I. V. & Rubio, A. Dielectric screening in two-dimensional insulators: Implications for excitonic and impurity states in graphene. *Phys. Rev. B* **84**, 085406 (2011).
67. Varsano, D., Palummo, M., Molinari, E. & Rontani, M. A monolayer transition-metal dichalcogenide as a topological excitonic insulator. *Nat. Nanotech.* **15**, 367 (2020).
68. Fujita, M., Machida, K. & Nakanishi H., Charge Density Waves under Magnetic Fields. *J. Phys. Soc. Jpn.* **54**, 3820-3832 (1985).
69. R. D. McDonald *et al.* Charge-Density Waves Survive the Pauli Paramagnetic Limit. *Phys. Rev. Lett.* **93**, 076405 (2004).
70. Mihály, G. & Canfield, P. C. Pinning energy versus order parameter in a charge-density-wave system. *Phys. Rev. Lett.* **64**, 459 (1990).
71. Fenton, E. W. Excitonic Insulator in a Magnetic Field. *Phys. Rev.* **170**, 816 (1968).



**Extended Fig. 1: Absence of structural phase transition near  $T = 100$  K.** **a**, Atomic-resolution image of the (010) surface captured by scanning transmission electron microscopy, demonstrating a consistent atom arrangement compared to pristine  $\text{Ta}_2\text{Pd}_3\text{Te}_5$  (010). **b**, Selected area electron diffraction patterns obtained from the focused-ion-beam cut lamella at  $T = 290$  K (top) and 90 K (bottom). The patterns exhibit identical crystal symmetry at both temperatures, indicating the absence of a structural phase transition in this temperature range. **c**, Atomic-resolution scanning transmission electron microscopy image of the (001) surface, revealing a consistent atom arrangement when compared to pristine  $\text{Ta}_2\text{Pd}_3\text{Te}_5$  (001). **d**, Selected area electron diffraction patterns acquired from the focused-ion-beam cut lamella at  $T = 290$  K (top) and 90 K (bottom). Akin to panel **b**, the patterns demonstrate the same crystal symmetry at both temperatures. The temperature-dependent selected area electron diffraction patterns provide evidence supporting the absence of a structural transition around 100 K.

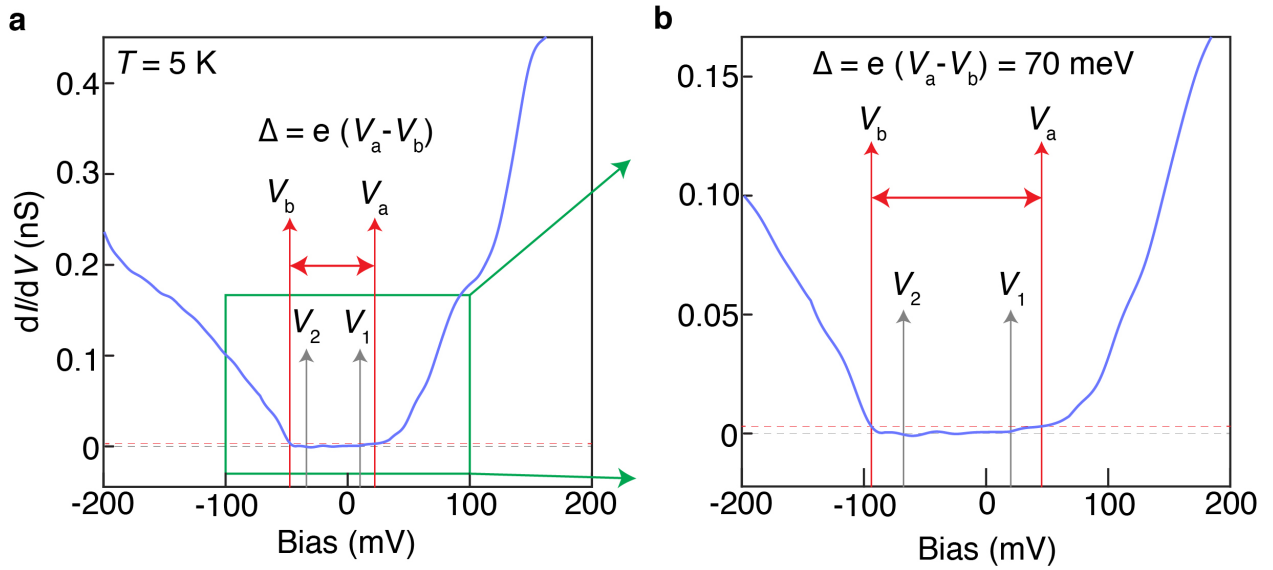


**Extended Fig. 2: Structure and phase characterization of Ta<sub>2</sub>Pd<sub>3</sub>Te<sub>5</sub>.** **a**, Atomic resolution image of the side surface, Ta<sub>2</sub>Pd<sub>3</sub>Te<sub>5</sub> (010), obtained through scanning transmission electron microscopy, displaying a consistent atom arrangement in comparison to pristine Ta<sub>2</sub>Pd<sub>3</sub>Te<sub>5</sub>. **b-i**, Elemental mappings of the side surface utilizing an energy dispersive X-ray detector. The mappings demonstrate the unperturbed atomic layers, highlighting the structural integrity and composition of Ta<sub>2</sub>Pd<sub>3</sub>Te<sub>5</sub>.

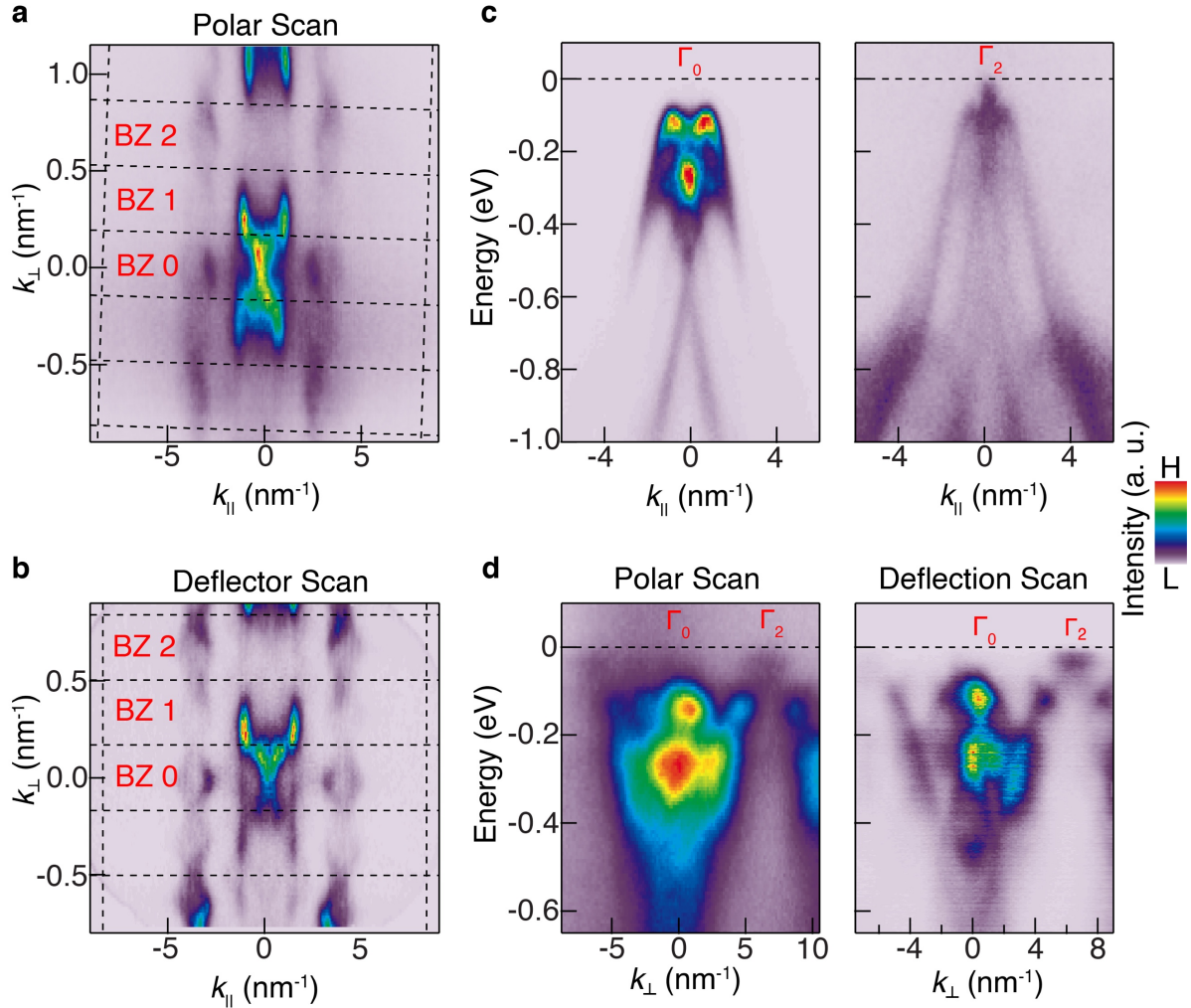


**Extended Fig. 3: X-ray diffraction measurements on  $Ta_2Pd_3Te_5$  revealing the absence of a structural phase transition as a function of temperature. a, X-ray diffraction pattern measured at exactly the same sample position**

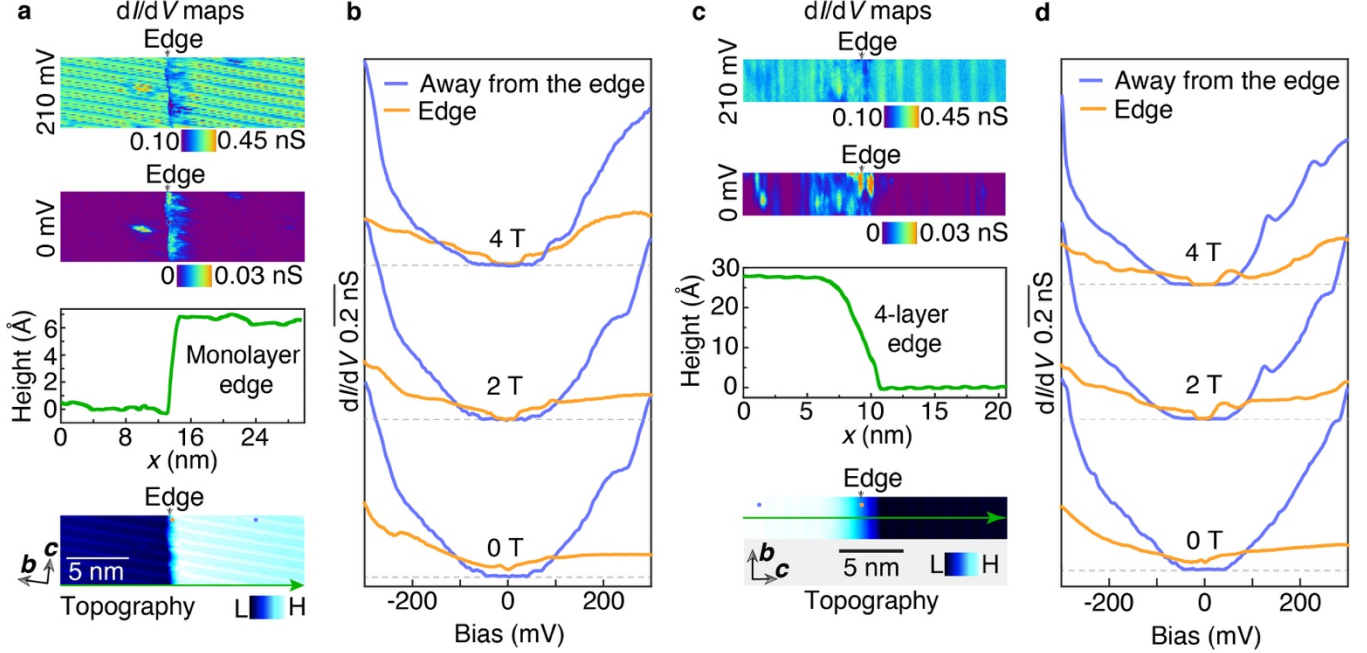
for different temperatures ranging from 300 K to 20 K. **b**, Maps along H-L obtained by summing over  $K = [-2.5, 3.5]$  measured at four temperatures. **c**, Maps along H-L obtained by taking a slice at  $K = [0.5, 1.5]$  measured at four temperatures. **d**, Maps along H-K obtained by summing over  $L = [-7.5, 20.5]$  measured at four temperatures. **e**, Maps along H-K obtained by taking a slice at  $L = [1.5, 2.5]$ . Notably, there is no appearance of any new or additional peak at low temperatures, and the X-ray diffraction measurements consistently exhibit a good agreement with the Pnma crystal structure at all the measured temperatures. This compelling evidence suggests the absence of a structural phase transition in  $\text{Ta}_2\text{Pd}_3\text{Te}_5$ .



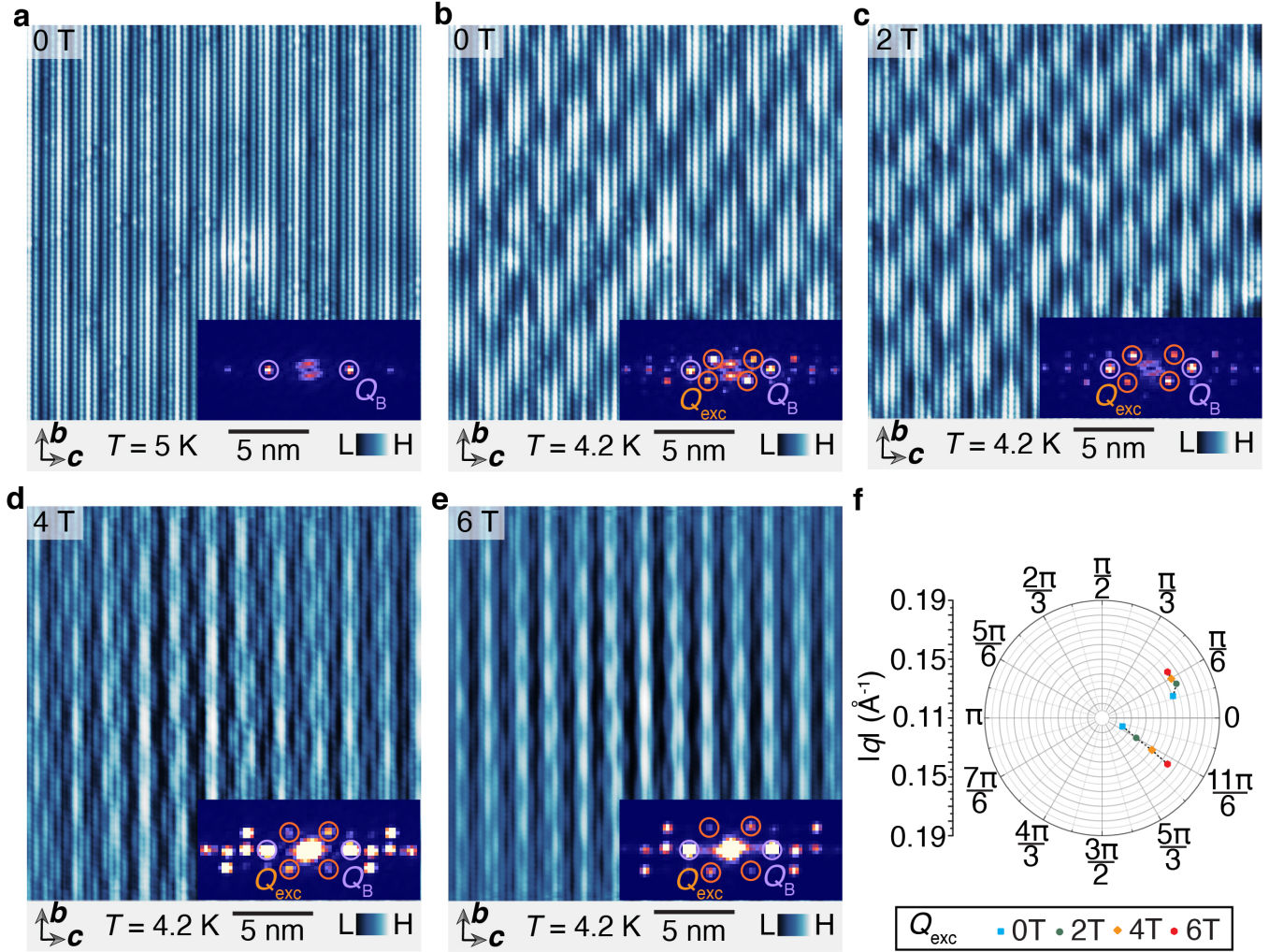
**Extended Fig. 4: Determination of the energy gap from tunneling spectroscopy.** **a**, Averaged  $dI/dV$  spectrum acquired by tunneling into the clean  $\text{Ta}_2\text{Pd}_3\text{Te}_5$   $bc$  plane at  $T = 5$  K. The voltage interval  $[V_1, V_2]$  is used to calculate the noise floor,  $\sigma$ . The dashed red line represents  $\Gamma = 2.36\sigma$ , which corresponds to the instrumental resolution of the  $dI/dV$  signal.  $V_a$  and  $V_b$  are the solutions of the equation  $dI/dV = \Gamma$ . The spectroscopic energy gap is calculated as  $\Delta = eV_a - eV_b$ , resulting in  $\Delta \approx 70$  meV in this case. **b**, Magnified view of panel **a**, focusing on the gapped region in the averaged  $dI/dV$  spectrum.



**Extended Fig. 5: Photoemission matrix element effects reveal states at the Fermi level.** **a,b**, Constant energy photoemission contours captured 600 meV below the Fermi level at  $T = 150$  K using polar (panel **a**) and deflection (panel **b**) mapping in the direction perpendicular to the analyzer slit ( $k_{\perp}$ ). Brillouin zones are labeled as BZ 0, BZ 1, and BZ 2. **c**, Photoemission energy vs. momentum cuts along the analyzer slit direction ( $k_{\parallel}$ ), traversing the  $\Gamma$  point in BZ 0 (left panel) and BZ 2 (right panel). **d**, Photoemission energy vs. momentum cuts perpendicular to the analyzer slit ( $k_{\perp}$ ), intersecting multiple  $\Gamma$  points. Similar behavior is seen in polar (left panel) and deflection (right panel) mapping with spectral weight extending to the Fermi level in BZ 2, but not BZ 0.

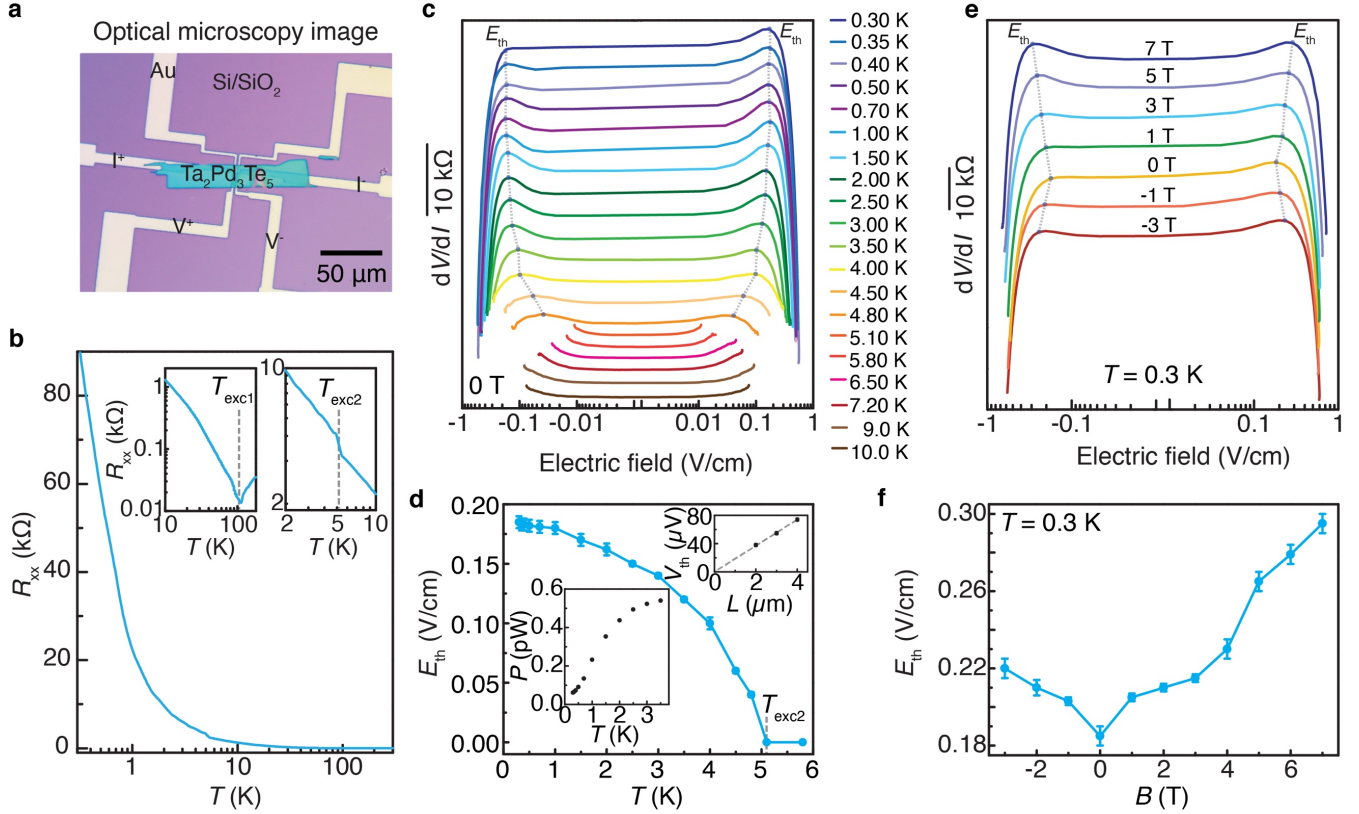


**Extended Fig. 6: Observation of time-reversal-symmetry-protected edge states in different edge configurations.** **a**,  $dI/dV$  maps acquired at different bias voltages (corresponding topography is shown in the bottom panel) around a monolayer step edge parallel to the  $c$ -axis measured at  $T = 5$  K. The height profile perpendicular to the  $c$ -axis is also displayed. The  $dI/dV$  map obtained within the energy gap ( $V = 0$  mV) reveals a pronounced edge state, whereas at  $V = 210$  mV, the edge state is suppressed. **b**, Tunneling spectra acquired at locations away from the step edge and on the step edge measured under various magnetic fields. The orange and violet curves represent the differential spectra obtained at the step edge and away from it, respectively. The corresponding spatial locations where the spectra are acquired are marked with color-coded circles on the topographic image in panel **a**. Spectra at different magnetic fields are taken at the same locations and are offset for clarity. Dashed horizontal lines mark the zero  $dI/dV$  for different fields. At  $B = 0$ , tunneling spectra reveal an energy gap around the Fermi energy away from the step edge, while a pronounced gapless, in-gap state is observed on the step edge. In contrast, at  $B = 2$  T and 4 T, the step edge state is suppressed, and an energy gap gradually develops with increasing magnetic field. **c**,  $dI/dV$  maps acquired at different bias voltages (corresponding topography is shown in the bottom panel) around a four-layer step edge parallel to the  $b$ -axis direction. The height profile perpendicular to the  $b$ -axis is also shown. The  $dI/dV$  map obtained within the energy gap ( $V = 0$  mV) reveals a pronounced edge state, whereas at  $V = 210$  mV, the edge state is suppressed. **d**, Tunneling spectra acquired at locations away from the step edge and on the step edge measured under various magnetic fields. The orange and violet curves represent the differential spectra taken at the step edge and away from it, respectively. The corresponding spatial locations where the spectra are acquired are marked with color-coded circles on the topographic image in panel **a**. Spectra at different magnetic fields are taken at the same locations and are offset for clarity. Dashed horizontal lines mark the zero  $dI/dV$  for different fields. At  $B = 0$ , tunneling spectra reveal an energy gap around the Fermi energy away from the step edge, while a pronounced gapless, in-gap state is observed on the step edge. In contrast, at  $B = 2$  T and 4 T, the step edge state is suppressed, and an energy gap gradually develops with increasing magnetic field. Tunneling junction setup:  $V_{\text{set}} = 300$  mV,  $I_{\text{set}} = 0.5$  nA,  $V_{\text{mod}} = 2$  mV.



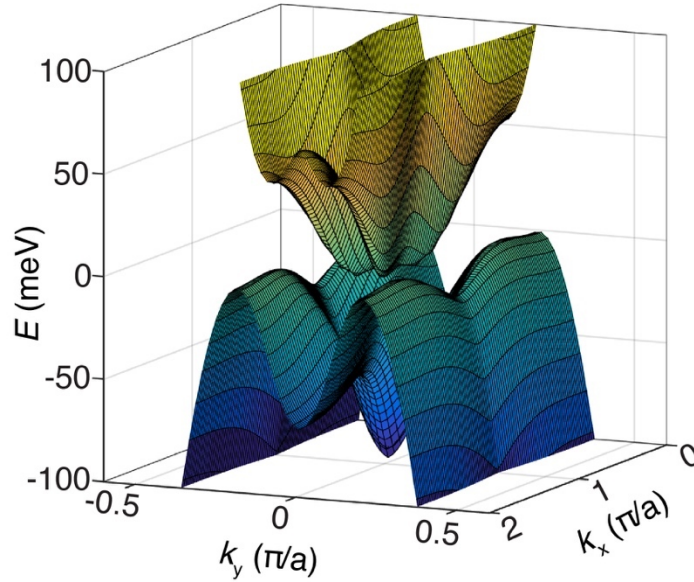
**Extended Fig. 7: Magnetic field tunability of the translation symmetry breaking order.** **a**, Atomically resolved topographic image of a clean Ta<sub>2</sub>Pd<sub>3</sub>Te<sub>5</sub> (100) surface acquired at  $T = 5$  K. Inset shows the corresponding Fourier transform image displaying well-defined Bragg peaks (purple circles). **b**, Topographic image of the same region presented in panel **a**, acquired at  $T = 4.2$  K and  $B = 0$  T, revealing a pronounced translation symmetry breaking order. Inset: Fourier transform image displaying well-defined superlattice peaks (orange circles) alongside the Bragg peaks (green circles). The extracted wavevector is  $Q_{\text{exc}} = [\pm(-0.43c^* + 0.035b^*), \pm(0.57c^* + 0.035b^*)]$ . **c**, **d**, **e**, Topographic images of the same location but acquired at magnetic fields 2 T, 4 T, and 6 T, respectively, highlighting a change in the translation symmetry breaking ordering pattern with the increasing magnetic field. The Fourier transform images shown in the inset reveal a gradually evolving  $Q_{\text{exc}}$  where  $Q_{\text{exc}}$  changes to  $[\pm(-0.44c^* + 0.051b^*), \pm(0.56c^* + 0.051b^*)]$  at 2 T,  $[\pm(-0.47c^* + 0.06b^*), \pm(0.53c^* + 0.06b^*)]$  at 4 T, and  $[\pm(0.5c^* + 0.07b^*)]$  at 6 T. **f**, Polar plot summarizing the magnetic field tunability of  $Q_{\text{exc}}$ . Starting from being incommensurate along both  $b$ - and  $c$ -axes at  $B = 0$  T,  $Q_{\text{exc}}$  evolves continuously and becomes commensurate along the  $c$ -axis at  $B = 6$  T. Tunneling junction set-up:  $V_{\text{set}} = 300$  mV,  $I_{\text{set}} = 0.5$  nA.



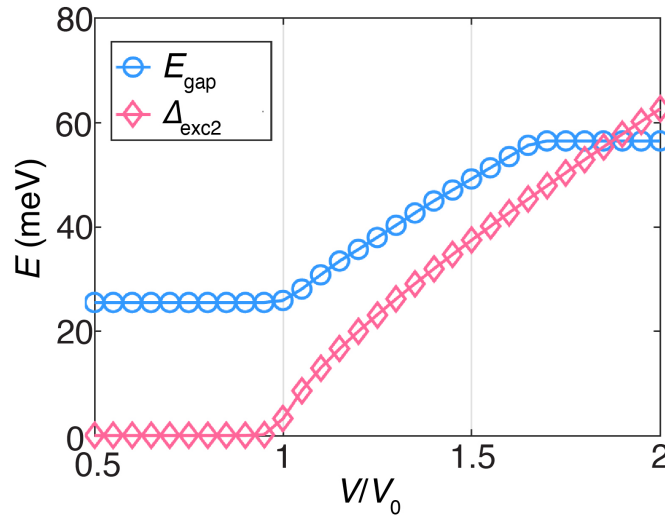


**Extended Fig. 8: Transport evidence for the translation symmetry breaking order.** **a**, Optical microscopy image of a four-point probe device (taken prior to its encapsulation with polymethyl methacrylate films) consisting of a mechanically exfoliated  $\sim 100$  nm thick  $\text{Ta}_2\text{Pd}_3\text{Te}_5$  flake, with marked current and voltage probes. **b**, Four-probe resistance ( $R_{xx}$ ) of the  $\text{Ta}_2\text{Pd}_3\text{Te}_5$  device as a function of the temperature,  $T$ . The insets display log-log plots of  $R_{xx}(T)$  in the temperature regions near the exciton insulator (left) and the finite momentum excitonic translation symmetry breaking (right) transitions, with corresponding transition temperatures,  $T_{\text{exc1}}$  and  $T_{\text{exc2}}$ , marked. Below  $T = 100$  K,  $R_{xx}$  shows a sharp increase in resistance, indicating insulating behavior due to the formation of the exciton insulator energy gap. Additionally, close to  $T = 5$  K,  $R_{xx}(T)$  exhibits a slight kink before continuing to increase with decreasing  $T$ . The onset of translation symmetry breaking order formation is marked based on the data in panels **c** and **d**. **c**, Differential resistance  $dV/dI$  as a function of electric field at various temperatures. Traces for different temperatures are vertically offset for enhanced clarity. At low electric fields,  $dV/dI$  remains constant for all temperatures. However, below the critical temperature  $T_{\text{exc2}}$ ,  $dV/dI$  sharply decreases above a threshold electric field  $E_{\text{th}}$ , indicating the onset of the collective phason mode or the electric field-induced sliding of the translation symmetry breaking order. ( $E_{\text{th}}$  is determined as the onset of the sharp decrease in  $dV/dI$  with respect to the electric field.) The circles mark the locations of  $E_{\text{th}}$  for each trace, both at positive and negative electric fields. **d**, Threshold electric field  $E_{\text{th}}$  as a function of temperature. The error bars represent the variation between positive and negative  $E_{\text{th}}$ .  $T_{\text{exc2}}$  denotes the temperature at and above which  $E_{\text{th}}$  becomes zero. Top inset: Plot of threshold voltage ( $V_{\text{th}}$ ) at  $T = 0.3$  K against the distance between the voltage contacts ( $L$ ), demonstrating a linear relationship, thereby validating the relationship  $E_{\text{th}} = V_{\text{th}}/L$ . Bottom inset: Temperature-dependent electrical power dissipation ( $P_{\text{th}}$ ) at  $E_{\text{th}}$ , obtained from  $P_{\text{th}} = V_{\text{th}}^2/[dV/dI(V_{\text{th}})]$ , demonstrating an increase in  $P_{\text{th}}$  with rising temperature, contrary to the thermally driven switching, thus supporting the intrinsic nature of the observed properties in  $\text{Ta}_2\text{Pd}_3\text{Te}_5$ . **e**,  $dV/dI$  as a function of electric field at various magnetic fields. Traces for different magnetic fields are

vertically offset for enhanced visibility.  $E_{th}$  (marked for each trace) changes with the magnetic field. **f**, Magnetic field dependence of  $E_{th}$ . The error bars denote the variation between positive and negative  $E_{th}$ . An external magnetic field is known to suppress the charge orders stemming from translation symmetry breaking<sup>68,69</sup> with the threshold electric field  $E_{th}$  being proportional to the amplitude of the translation symmetry breaking order parameter<sup>70</sup>. Therefore, the contrasting increase of  $E_{th}$  as a function of  $B$  can be understood as resulting from the progressive, field-induced commensurability of  $Q_{exc}$  with the lattice constant along the  $c$ -axis (Fig. 4).



**Extended Fig. 9: Low-energy band structure of monolayer  $Ta_2Pd_3Te_5$  obtained from first-principles calculations.**



**Extended Fig. 10. Strength of the finite momentum excitonic translation symmetry breaking order  $\Delta_{exc2}$  (red) and bulk gap  $E_{gap}$  (blue) as functions of interaction strength  $V$ .  $V_0 = 1.25$  eV and the other parameters are identical to those presented in Fig. 5.**

**Competing interests:** The authors declare no competing interests.

**Data and materials availability:** All data needed to evaluate the conclusions in the paper are present in the paper. Additional data are available from the corresponding authors upon reasonable request.

**Acknowledgement:** Experimental and theoretical work at Princeton University was supported by the Gordon and Betty Moore Foundation (GBMF4547; M.Z.H.). The material characterization is supported by the United States Department of Energy (US DOE) under the Basic Energy Sciences program (grant number DOE/BES DE-FG-288 02-05ER46200). Crystal growth at Beijing Institute of Technology is supported by the National Key Research and Development Program of China (grant nos 2020YFA0308800 and 2022YFA1403400), the National Science Foundation of China (grant no 92065109), and the Beijing Natural Science Foundation (grant nos Z210006 and Z190006). L.B. is supported by DOE-BES through award DE-SC0002613. The National High Magnetic Field Laboratory (NHMFL) acknowledges support from the US-NSF Cooperative agreement Grant number DMR-DMR-2128556 and the state of Florida. We thank T. Murphy, G. Jones, L. Jiao, and R. Nowell at NHMFL for technical support. T.N. acknowledges supports from the European Union's Horizon 2020 research and innovation programme (ERC-StG-Neupert-757867-PARATOP). Z.W. thanks the Analysis and Testing Center at BIT for assistance in facility support. Y.Y.P. is grateful for financial support from the National Natural Science Foundation of China (11974029).